Pop-up Langmuir probe diagnostic in the water cooled divertor of Wendelstein 7-X

A. Pandey ✉ ⓘ ; S. Bohm; A. Carls ⓘ ; C. Cordes; M. Endler ⓘ ; J. Fellinger ⓘ ; S. Freundt ⓘ ; K. Gallowski;
K. Hammond ⓘ ; D. Hathiramani ⓘ ; G. Isberner; J. P. Kallmeyer; M. Krause; J. Kügler; M. Otte ⓘ ;
T. S. Pedersen; D. Rondeshagen; J. Ruhnau; T. Schröder ⓘ ; T. Sieber ⓘ ; J. Wendorf; W7-X Team

Check for updates

View Online

Export Citation

Pop-up Langmuir probe diagnostic in the water cooled divertor of Wendelstein 7-X

View Online   Export Citation   CrossMark

A. Pandey,[1,a] (iD) S. Bohm,[1] A. Carls,[1] (iD) C. Cordes,[1] M. Endler,[1] (iD) J. Fellinger,[1] (iD) S. Freundt,[1] (iD) K. Gallowski,[1] K. Hammond,[2] (iD) D. Hathiramani,[1] (iD) G. Isberner,[1] J. P. Kallmeyer,[1] M. Krause,[1] J. Kügler,[1] M. Otte,[1] (iD) T. S. Pedersen,[3] D. Rondeshagen,[1] J. Ruhnau,[1] T. Schröder,[1] (iD) T. Sieber,[1] (iD) J. Wendorf,[1] and W7-X Team[b]

AFFILIATIONS

[1] Max-Planck Institut für Plasmaphysik, Greifswald 17491, Germany
[2] Princeton Plasma Physics Laboratory, Princeton, New Jersey 08540, USA
[3] Type One Energy, Madison, Wisconsin 53703, USA

[a] Author to whom correspondence should be addressed: arun.pandey@ipp.mpg.de
[b] See the author list of O. Grulke *et al.*, Nucl. Fusion (to be published) (2024).

ABSTRACT

The design, development, and successful implementation of pop-up Langmuir probes installed in the water-cooled divertor of W7-X are described. The probes are controlled by drive coils (actuators) installed behind the divertor plates. These drive coils make use of the magnetic field in W7-X to move the probe tips into and out of the plasma. The drive coils were installed in the vacuum vessel after extensively testing the durability of the coils and analyzing the criteria for safe operation. The probe design is carefully tailored for each of the 36 probe tips in order to be suitable for the different magnetic field configurations used in W7-X and ensure that the probes do not present leading edges to the magnetic flux tubes. An electronic bridge circuit is used for measurement to compensate for the effects of signal propagation time on the long cable lengths used. The diagnostic is integrated with the segment control of W7-X for automated operation and control of the diagnostic. The evaluation of the results from the plasma operation is presented after accounting for appropriate sheath expansion for negative bias voltage on the probes.

I. INTRODUCTION

The Wendelstein 7-X stellarator[1] has been upgraded with new water-cooled divertors to facilitate extended pulse operations. These operations are dependent on the conditions in a divertor plasma, emphasizing the importance of accurately measuring the local plasma parameters. For this purpose, a Langmuir probe diagnostic, which is one of the widely used diagnostics for local plasma measurements,[2–4] is installed in the upgraded divertors in W7-X. Langmuir probes are cost-effective and reliable plasma diagnostics for local measurements of plasma parameters, such as electron temperature, plasma density, floating potential, and the ion flux impacting the divertor.[4,5] Due to specific considerations outlined in this paper, Wendelstein 7-X[1] is equipped with a new set of pop-up divertor Langmuir probes for Operation Phase (OP) 2. In the previous operation phase (OP 1.2) of W7-X, test divertor units

(TDUs) made of fine grain graphite were used,[6] which had almost flush mounted graphite Langmuir probes.[7,8] In OP 2, new High Heat Flux (HHF) divertors, with the same shape and size as the TDUs, are installed in W7-X,[9] as the device is being prepared to run longer discharges with higher heating power as compared to the previous OP. The divertors must also be prepared to handle high heat fluxes for extended intervals of time, and therefore, the TDUs are replaced with the water-cooled carbon fiber-reinforced carbon (CFC) divertors.[9,10] As it would have been impractical to actively cool the probe tips, the probes would not be able to withstand the expected plasma power loads for the full discharge duration. It was therefore planned to drive the probes into and out of the plasma during the discharge.

The reciprocation of the probes is done using actuators installed behind the divertors. Two probes are operated by each actuator. Rather than having a single pneumatically controlled recip-

rocation mechanism for a larger number of probes, as usually employed for fast reciprocating probes in fusion experiments,[11–13] multiple drive coils are used. This facilitates keeping the probes in the same position relative to the target surface despite of thermal deformation of the target plates. The target surface in W7-X, ranging from the innermost (inboard) to the outermost (outboard) probes, is not uniformly flat. It is crucial that the insertion and retraction paths of the probes remain clear of the edges of the holes where they are installed. When probes in a divertor are linked to a single actuator, their positions and orientations must be carefully designed to ensure this unobstructed path. Consequently, the trajectories of different probes may slightly diverge in angle. Minor distortions in the target could create blockages in a probe's path, an issue that becomes more pronounced when multiple probes are connected to one actuator. Such obstructions not only hinder the affected probe but can also complicate the operation of the others. While this risk is present even with two probes per actuator, it escalates significantly with a higher number of probes per actuator. The present design also gives an advantage of controlling each pair of probes independent of the other probes so that in case of an accidental event leading to an incomplete retraction of one of the probes, other drive coils remain unaffected.

The flush mounted TDU Langmuir probes used in the previous OP had a faceted design such that the angle of incidence of a magnetic field on the probe tip surface was ~3° – 6° for the magnetic field configurations used. At such small angles, the interpretation of the Langmuir probe data is difficult because of the non-saturation of ion current[2,4,14–16] and modifications of the sheath structure above the probes.[17,18] The newly designed pop-up Langmuir probes have a greater magnetic field incidence angle (≥24°) at their tips, which mitigates issues related to altered ion flux at lower angles.[14,18,19] These probes are exposed to plasmas for a brief duration, leading to a lower temperature increase compared to continuously exposed flush-mounted probes. Despite receiving higher heat flux due to the larger angle, their short exposure duration allows for sufficient cooling. However, this increased heat flux necessitates careful selection of probe materials and limits the duration of plasma exposure. In the present context, a probe tip with a greater angle of the magnetic field incidence also presents a larger projected area to the magnetic field. However, given that the probe tips are small, even though their incidence angle exceeds that of flush-mounted probes, the increase in projected area is not substantial enough to significantly elongate the ion collection length. According to the estimate given in Ref. 20, for a probe of 1 mm thickness, the ion collection length would be on the order of ~1 m.

The pop-up probe concept previously used in JET[21] and Alcator C-mod[22,23] is therefore adopted due to all the considerations mentioned above. This paper is structured as follows: Sec. II details the configuration of the discontinuous divertor modules in W7-X and the positioning of probes in the divertor. Section III describes the design principles of the actuators used in the diagnostic system. Section IV provides an overview of the criteria for selecting probe materials, with Sec. V addressing the potential risks associated with using high-Z materials. The rationale and limitations in determining the probe dimensions are discussed in Sec. VI. Comprehensive testing of the probe and actuator assembly for qualification purposes is covered in Sec. VII. As Secs. II and III illustrate the necessity of running a current through the actuator, Sec. VIII presents a thorough calculation of this current. The operations of the actuators and probes are explored in Secs. IX and X, respectively. Section XI focuses on the diagnostic performance during plasma experiments at W7-X. Section XII introduces a method for calculating the probe's effective area exposed to magnetic flux tubes in a plasma environment, along with the analysis of the resulting data. This paper concludes with a summary in Sec. XIII. An in-depth account of the probe dimension calculations is provided in the Appendix.
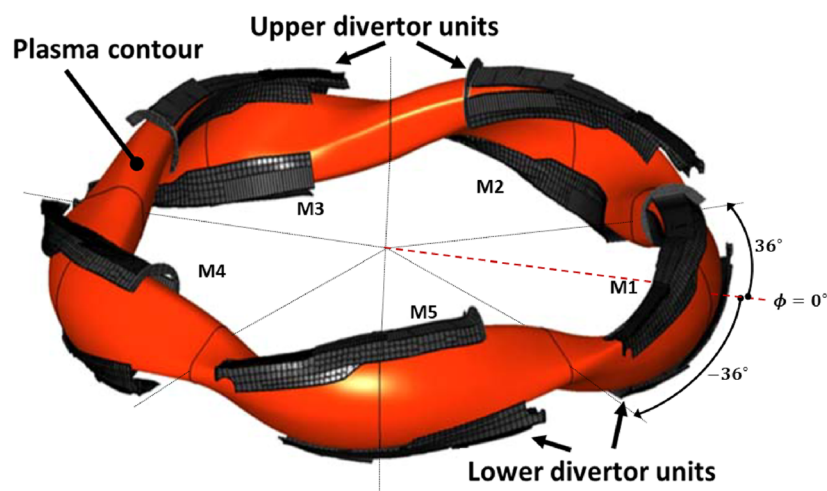

FIG. 1. CAD model of the ten divertor locations and the last closed flux surface. The five modules of W7-X have been labeled from M1 to M5. The toroidal angle $\phi = 0$ has been marked for reference.

II. W7-X HHF DIVERTOR

Magnetic field configurations used in W7-X have a low shear and a rational rotational transform value at the edge creating stable edge magnetic islands. These islands act as natural sections of the plasma that intersect with the divertor plates. W7-X has five toroidal modules (Fig. 1) with non-planar and planar coils to generate the required magnetic field with a desired rotational transform. The five modules have been designed to have identical magnetic surfaces, and therefore, W7-X exhibits five-fold toroidal symmetry. The divertor in W7-X has ten separate "divertor units" (DUs), as shown in Fig. 1, consisting of vertical and horizontal targets. Each of the five toroidal modules of W7-X has an upper and a lower DU. Each horizontal divertor is divided into nine Target Modules (TMs) from TM1h to TM9h. Each target module has several target-elements (TEs) or divertor fingers. In this paper, we focus on one specific toroidal module—module 5, as shown in Fig. 2, where the Langmuir probe system is installed in the upper and lower horizontal divertor units. Only the divertor units in this particular module have Langmuir probes (LPs), and thus, this paper solely references the upper horizontal divertors (UDs) and lower horizontal divertors (LDs) of module 5. The plasma-facing surfaces of W7-X are categorized based on the heat load they experience during experiments. Areas with lower heat loads are covered with stainless steel panels, moderately exposed areas are covered with graphite tiles, and the highest loads are sustained by the CFC targets.[24,25] The pop-up probe assemblies are installed behind three divertor target-elements in each divertor unit, as shown in Fig. 2. The probes could not be installed on an arbitrary target-element because of the space constraint from the cooling water-pipes behind the divertor. Thus, the probes could only be installed in either the first or the last target-element of a target module.

The position of the line with a highest power load (strike line) on the divertor depends on the magnetic field configuration used for experiments in W7-X, determined by the currents in the field coil circuits and the plasma current.[26,27] The location of the pop-up Langmuir probes is chosen such that some probes are always at the strike line location or close to the strike line location on the divertor for all the magnetic field configurations. The probes in TM2h and TM3h (six probes + eight probes) shown in Fig. 2 are installed almost at the same toroidal angle $\phi = -82.4°$ for LD probes and

$\phi = -61.5°$ for the UD probes. In total, there are 14 probes in this section of the divertor, as shown in Fig. 3(a). The magnetic surfaces of the island are shown in Fig. 3(a) for a "standard configuration" (edge $t = 1$) vacuum field. There are four probes in TM8h, shown in Fig. 3(b) ($\phi = -56.8°$ for LD and $\phi = -87.1°$ for UD), for monitoring the divertor plasma in the "high iota" configurations[28] in W7-X where edge $t > 1$. The magnetic surfaces shown in Fig. 3(b) are from a configuration with edge $t = 5/4$.

III. DESIGN CONCEPT

The probes are installed in the regions where, in certain magnetic configurations, high heat fluxes parallel to the magnetic field (of up to ~200 MW/m^2) can occur. The heat flux deposited on the probe tip depends on the angle at which the magnetic field is incident at the probe tip. While this incidence angle varies for each probe, its value is around ~24°. Consequently, the heat flux deposited on the probe tip is estimated to be roughly half of the parallel heat flux due to this angular orientation. Only high-temperature resistant materials (e.g., tungsten or graphite) with good electrical conductivity are suitable for operation under these circumstances. Even these materials cannot cope with such excessive power densities in continuous operation, but can only be driven into the plasma edge for a short time (~50 ms) and then have to be pulled back into a retracted position. It was therefore necessary to develop a fast probe driving mechanism that is also sufficiently compact to be installed behind the divertor. This is done using the concept of a "magnetic see-saw." We call the assembly of different components required for moving the probe a drive unit. The primary component of the drive unit is a rigid coil, used as an actuator, with the freedom to rotate about an axis almost perpendicular to the W7-X magnetic field (Fig. 4). The coil is made of 110 turns of gold wire, housed in a rectangular ceramic annulus. When current $\mathbf{J}$ is run through the coil, the Lorentz force $\mathbf{J} \times \mathbf{B}$ due to the W7-X magnetic field will generate a torque on the coil and cause the coil to rotate. This is schematically shown in Fig. 4, where a magnetic field B results in a force F in the arms of the coil where the current J in the coil is perpendicular to the field. If the coil is mechanically connected to one or more probes, applying a current to the coil will drive them into the plasma or out of the plasma depending upon the polarity of the current. It is crucial to
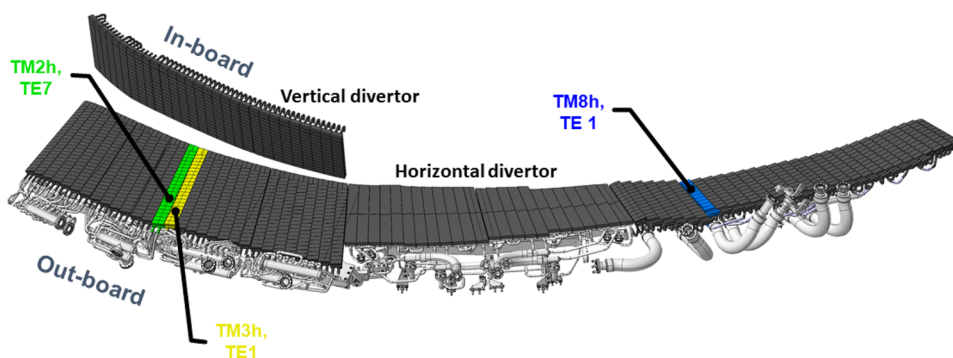
FIG. 2. CAD model of the W7-X HHF divertor unit (lower) in toroidal module 5 showing the locations of the divertor probes.
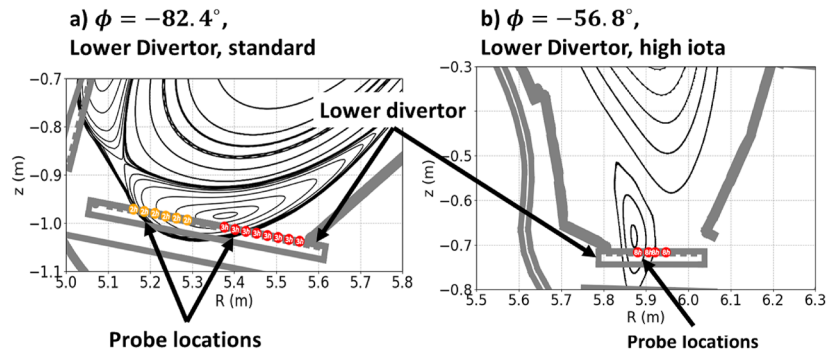
FIG. 3. The pop-up probe locations in the lower divertor target module at (a) $\phi = -82.4°$ with the flux surfaces in the standard magnetic field configuration. TM-2h probes are shown in orange, while TM-3h probes are in red. (b) $\phi = -56.8°$ with the flux surfaces in the high-iota configurations.
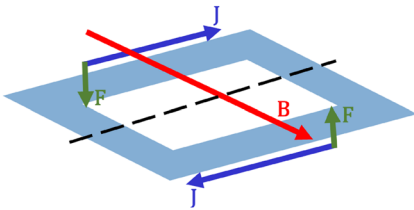

FIG. 4. Schematic of the concept on which the drive units are based, with vectors indicating magnetic field B, current J in the coil, and Lorentz forces F exerted on the coil when it carries current.

note that the drive unit will not function in the absence of the W7-X magnetic field and the direction of the current in the drive unit must be reversed if the W7-X magnetic field direction is reversed. The calculation of the current that should run through the coil for moving the probe either downward or upward will be shown in Sec. VIII.

The computer aided design (CAD) model of one such drive unit for the upper divertor is shown in Fig. 5. The important components are labeled in Fig. 5. The electrical connections to the two terminals of the drive coil and the two probe holders are provided through separate CuBe strips. The drive unit is equipped with stoppers that allow for an axial movement of 5 mm. Each unit features two sets of stoppers, one for each probe holder. In the fully retracted state, the coil is held in its parking position by the retraction stoppers. During the insertion process, the coil moves until it reaches the insertion stoppers. This setup ensures a consistent stroke length of ~5 mm for each probe. Consequently, for each specific probe, the fully inserted and retracted positions remain constant and were accurately determined following the installation of the probe in the probe holders. There are two springs on the drive unit, namely, (1) push-spring or compression-spring, which pushes the drive unit on the back of the target plate, and (2) a pull-spring, which holds the drive unit in place and attached to the target at all times. Both the springs can exert a force greater than 25 times the force required to keep the drive unit fixed. This is especially important for the lower divertor drive units, where the weight of the drive unit is acting against the action of the push-spring. The two springs together help to fix the drive unit in its

place while at the same time decoupling the drive unit from the possible deformation of the target plate. From a safety point of view, it is important that the probes remain in the parked position (retracted position) in the divertor when no voltage is applied to the drive coil. Therefore, there should be a mechanism for the passive retraction of the probes to the parked positions. The lower divertor probes move against gravity during insertion. The weight of the tungsten probes allows for the passive retraction without using any additional component, whereas, in the case of the upper divertor probes, the probes move downward during insertion and against gravity during retraction. Therefore, a counterweight on the opposite (to probes) side of the coil is attached to the coil, as shown in Fig. 5. This would be called counter-probe side of the coil in the rest of this paper.

A picture of two installed drive units behind the divertor without the probes is shown in Fig. 6. To protect the coil and probe connections from electron cyclotron resonance heating (ECRH) stray radiation, a copper-coated stainless-steel shield is installed over the coil (not shown in Fig. 6) and the probe-holders. For each coil, the probe-holders are behind the two ECRH shields in Fig. 6. Two probe-holders are attached to each coil, as shown in Figs. 5 and 6. Each probe is held in place tightly by the probe-holder. The engineering drawing of a probe is shown in Fig. 7 with the lengths shown in mm. The rear end of the probe has a wedge shape for easy insertion into the probe-holder. The probe has a trapezoidal "pit"-like structure, which acts like a socket for the holder-pin inside the probe holder. The dimensions of the wedge and the trapezoidal "pit" have been precisely chosen to guarantee a good electrical connection between the holder pin and the probe; it will be discussed in more detail shortly. Additionally, these dimensions are designed to exert enough force to maintain the probe's stability in its position. Figure 7 demonstrates the necessity for such exact dimensions. As shown in Fig. 7(a), the upper half of the probe (containing the probe tip) has a diameter of 1.96 mm with a strict maximum tolerance of -0.02 mm, whereas the lower half has a diameter of 2 ± 0.05 mm. The probe tip has a fin of thickness 1 mm [Fig. 7(b)], which is the part of the probe that is exposed to the plasma. The design of the fin is customized for each probe such that the magnetic flux tube does not make a contact with the straight edge of the probe tip (see the Appendix).
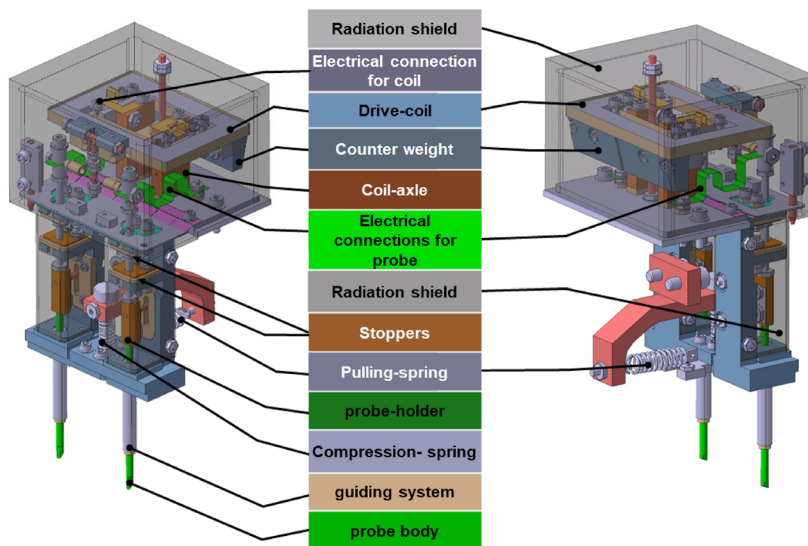
FIG. 5. CAD models of the drive coil assembly from two viewing angles showing different components of the assembly.

The design of the probe-holder with a probe is shown in Fig. 8. The probe-holder contains a movable holder-pin as shown in Fig. 8, which creates a snap-lock for the probe. The probe can be pushed inside the probe-holder while pushing the holder-pin upward (to the right in Fig. 8). The location and dimensions of the "pit" in the probe and the holder pin in the probe-holder are decided such that the pin rests on the rear sloping edge of the pit when the probe is fully inserted, as shown in Fig. 8(b). This ensures a tension is maintained in the Inconel spring, which presses the probe against the probe holder. This is important because the electrical connections to the probe are through the Inconel spring and the probe holder. This mechanism holds the probe firmly in place during the motion of the probe-holders along the probe axis during operation. A bayonet lock mechanism is designed on the probe tip to remove/place the probe from/into the probe-holder [Fig. 8(e)]. To remove the probe from the probe-holder, an exchange tool or removal tool, which is a steel tube with a small pin attached to its internal surface [Fig. 8(d)], is mounted on the bayonet mount slot designed in the probe tip. The probe is rotated with the help of the exchange tool such that the flat side of the probe is facing the pin inside the holder Fig. 8(c). At this point, the probe can simply be pulled out of the drive unit.

IV. PROBE MATERIAL

As stated earlier, due to the high heat fluxes expected on the probes tips ($Q_{\parallel} \sim 100$–200 MW/m^2), only high temperature resistant materials (graphite, tungsten, molybdenum, or alloys with similar properties), which are electrically conducting, can be considered for constructing the probes. These constraints on the probe material narrowed down the choice of the material to W (tungsten), Mo (molybdenum), and graphite. Very thin ($\sim$2 mm) graphite rods are prone to damage and breaking because of the brittleness of graphite. The design of the probe tips with a bayonet mount would have been difficult to make on graphite probe tips. Furthermore,

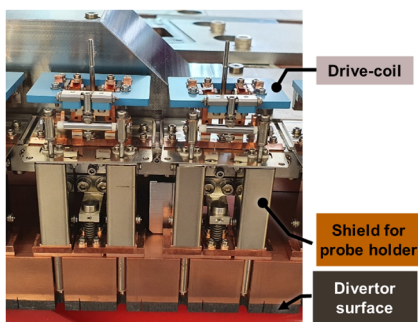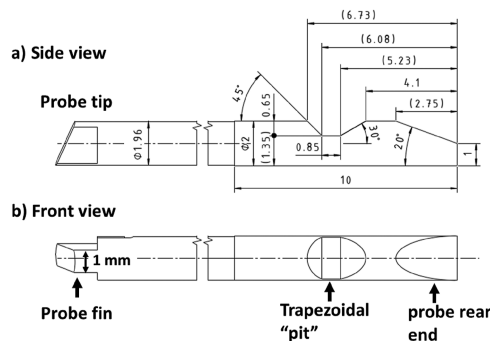**FIG. 6.** Installed drive units behind the HHF-divertor.

FIG. 7. Engineering drawing of a probe. The probe tip has slightly different dimensions for each probe. (a) Side view of the probe tip showing the dimensions of different parts of the probe. All the lengths shown are in mm. (b) The front view of the probe showing the shapes of the probe fin, trapezoidal "pit," and the wedge-shaped rear end of the probe.
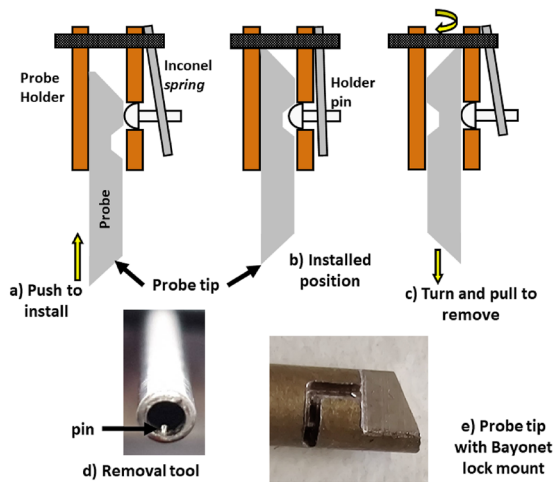
FIG. 8. Design of the probe-holder, probe tip, and the removal tool is shown. (a)–(c) Description of the procedure to install a probe in the probe-holder and remove the probe from the probe-holder. (d) The removal tool with a pin to go in the bayonet lock mount on the probe tip shown in (e).

graphite has a lower thermal conductivity as compared to Mo and W. Tungsten is a better choice if one considers the melting point of W (3700 K) and Mo (2900 K). However, both W and Mo have comparable thermal conductivities. Therefore, heat handling capabilities of Mo and W probes were simulated and compared to arrive at the final probe material. In the simulations carried out for heating of the probe in the presence of a high heat flux ($Q_\parallel \sim 50$–200 MW/m^2), it was found that there was a significant difference in the peak temperatures reached during plasma operation between W probe tips and Mo probe tips. The W probes could be held in the plasma for much longer without reaching the melting temperature of tungsten. Due to these reasons, tungsten was chosen for manufacturing of the probes. However, there are safety aspects associated with the use of a high-Z material, such as W or Mo in the plasma. Such high-Z impurities can lead to plasma collapse even when they are present in trace amounts in the plasma. A brief analysis of such a scenario is presented in Sec. V.

V. RISK ASSESSMENT FOR TUNGSTEN PROBE TIPS

Tungsten has a high atomic number (Z = 74), and even a small concentration of tungsten impurity ($n_W/n_e = 10^{-5}$) can lead to a radiation collapse of the plasma.[29] Therefore, it is crucial to conduct a risk assessment of the probe reciprocation system. The purpose of this risk analysis is to assess excessive exposure of the probes to the plasma, as over-exposure can cause evaporation of the probe tips. This can result in the release of impurities into the plasma, leading to degraded or failed experiments. Potential causes of over-exposure include mechanical failure of divertor-mounted components or operator error in setting drive unit control waveforms. To minimize the risk, the drive unit is designed with counterweights to keep the probes retracted when there is no current through the coil. All components are qualified to withstand at least 4×10^5 reciprocation

cycles (see Sec. VII). The exposure time limits are determined through finite-element thermal modeling.

In the unlikely event, where a drive coil is not able to retract the probes, two probes would be exposed to the plasma. A very conservative estimate, where the stuck probe tips are completely evaporated after receiving a parallel heat flux of 200 MW/m^2, is made. For a plasma density of 10^{19} m^{-3} and an electron temperature of 1 keV (W radiation peaks at ~1 keV), a total of 36 discharges would be required to get rid of the tungsten, assuming that all of tungsten from the probe tips would go inside the plasma core after subtracting the prompt redeposition fraction[30] on the divertor. This means that even if we do get such an accumulation of tungsten in the core while the two probe tips are being evaporated during each shot until the shot is disrupted, we could get rid of the stuck tungsten probe tips by running about 36 or less high-power, low density discharges.

In plasma discharges where radiation from the plasma core is more prominent than radiation from the plasma edge, the onset of a radiative collapse starts already at a radiation level of >60% heating power, needing twice the number of pulses for cleaning. In this context, it should be mentioned that before the threshold radiation levels for radiative collapse are reached, the radiation cooling might also simultaneously result in a strong reduction of the target loads, reducing the evaporation rate and, consequently, increasing the time until the necessary W-concentration for significant radiation. This can lead to two scenarios: (a) the W-source becomes so low that within the usual pulse duration of W7-X no collapse will be achieved and no severe energy degradation is visible or (b) in the case of predominant plasma core radiation and finite W confinement, a "medium" W-source allows a stationary radiation level below 60% of the heating power without a radiative collapse but with a stably degraded plasma energy. In case (a), it can take a long time (many discharges) to completely evaporate the tips, but, on the other hand, the W-radiation seems not to limit the experimental program. However, in case (b), the experimental program can be affected by W-radiation depending on the radiation level without limiting the pulse length by radiative collapse. This makes simple estimations a little bit more complicated.

Some experiments have been performed in tokamaks to estimate a scenario like the one in question. In one such experiment performed in ASDEX Upgrade with sublimation probes near the divertor (at the bottom),[31] the probability that the tungsten impurity would enter the scrape-off layer (SOL) was found to be 6%. In another such experiment with tungsten pins in the outer divertor of ASDEX Upgrade, the fraction of tungsten that goes into the core was measured to be only 0.16% of the total amount of W-atoms released from the pin.[29] If we consider such a retention for the case of W7-X as well, we would end up with a density of tungsten in the core, which can be calculated as

$$n_{W,core} = n_{W,probe} \times (1 - f_{red}) \times (0.16/100)$$
$$= 2.1 \times 10^{18} \times (1 - 0.53) \times 0.0016$$
$$= 1.57 \times 10^{15} \, m^{-3}, \tag{1}$$

where $n_{W,probe}$ is the number of tungsten atoms released from the probe divided by the volume of the plasma and f_{red} is the redeposited fraction. f_{red} redeposition depends on the ratio of the ionization

03 May 2024 14:53:03

length and the ion Larmor radius: $\gamma_P = \lambda_{iz}/\rho_i$ and can be computed from the relation given in Ref. 30,

$$f_{red} = 1/2[\exp(-2\gamma_P) + \exp(-\gamma_P/5)]. \quad (2)$$

For the present case, we assume the values given in Ref. 32 for the temperature of tungsten atom ~4.4 eV. In the magnetic field of W7-X, the Larmor radius of tungsten ~1.7 mm for a singly charged tungsten atom. Ionization length $[\lambda_{iz} = v_W/(\sigma_{ion}v_e n_e)]$ for tungsten ~1.3 mm, computed for $T_e = 20$ eV, $n_e = 2 \times 10^{19}$ m^{-3}, $\sigma_{ion}v_e = 7.9 \times 10^{-14}$ m^3 s^{-1},[33] and $\gamma_P = 0.764$. v_W and v_e are the thermal velocities of tungsten atoms and electrons, respectively.

Taking an example of a typical hydrogen plasma discharge in W7-X with an input power of 4 MW with $n_e = 5 \times 10^{19}$ m^{-3} and $T_e = 4$ keV, radiated power by tungsten density $n_W = 1.57 \times 10^{15}$ m^{-3} in the core is $n_e n_W L_z(T_e)$. $L_z(T_e)$ is the radiation cooling rate,[34]

$$L_z(T_e) = \Sigma_i(A_i[\log_{10}(T_e)]^i). \quad (3)$$

The values of the A_i coefficients are given in Ref. 34. The radiated power comes out to be 0.411 MW, which is 10.2% of the total input power. Therefore, we can conclude that this much accumulation of tungsten is too small to kill the discharge[26] but could radiate away a small fraction of input power depending upon electron density and temperature in the core. In the case of tokamaks, the evaporation of tungsten interferes with the plasma startup because in tokamaks the current build-up is important for confinement as well, but for an optimized stellarator, such as W7-X, this might not be the case. This is a very conservative estimate because we are considering a complete accumulation of tungsten, which is coming out of the probes after re-deposition, into the core without considering impurity transport. Nevertheless, such a situation has not been experimentally investigated in the case of an optimized stellarator, such as W7-X.

VI. PROBE DIMENSIONS

The divertor geometry in W7-X is designed such that the magnetic field makes a grazing incidence at the target plate. Some of the first and last target-elements of each target module have chamfered edges to avoid any leading edge. The probes are installed in the last target-element of target-module 2h and first target-element of target-module 3h where such chamfered edges exist (Fig. 2). This creates a situation where, depending on the length of the probe, a part of the probe tip may be shadowed by the chamfered edge or pose an unacceptable leading edge to the magnetic flux tube. Therefore, the length of the probe must be adjusted according to the magnetic field configuration where the length of the straight edge of the probe presented to the magnetic field is maximum. This configuration would be called the most critical field configuration. The most critical field configuration can be different for each probe. An example of the probe installed in such a chamfered edge is shown in Fig. 9.

The location in the plane of the divertor surface at the center of the aperture for the probe in the divertor is referred to as the penetration point and is marked as P in Fig. 9. The probe axis passes through P. The probe tip has a triangular fin, with its diagonal face inclined at an angle ψ with respect to the base of the fin shown as
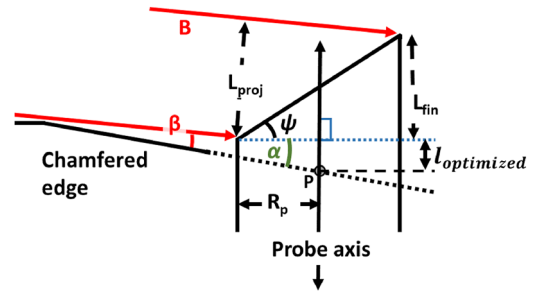

FIG. 9. Schematic of the probe tip showing the face of the probe seen by the magnetic field.

a blue dotted line in Fig. 9. The angle between magnetic field and divertor surface is β. The angle between the probe axis and divertor surface normal is α such that the projected length of the probe face is $L_{proj} = 2R_P \sin(\psi - \alpha + \beta)/\cos(\psi)$, where R_P is the radius of the probe. $L_{fin} = 2R_P \tan(\psi)$ is the length of the fin on the probe tip (see the Appendix for the calculation). The probe lengths were calculated based on the following considerations:

(1) The probes must not present a leading edge to the magnetic field line in their inserted positions.
(2) The projected length of a probe tip in the vacuum field should be $\leq (1 \pm 0.1)$ mm.

Figure 10 shows a schematic showing a probe in its retracted and inserted positions; the depth of the probe-holder (L_{depth}) from a divertor surface (from point P) in the inserted position along the axis of the probe was measured along with the stroke length (L_{stroke}) of each probe for each probe location after the installation of the drive units behind the divertor. Stroke length is the distance traveled by the probe tip from a fully retracted position to the fully inserted position. The total probe length consists of three lengths,

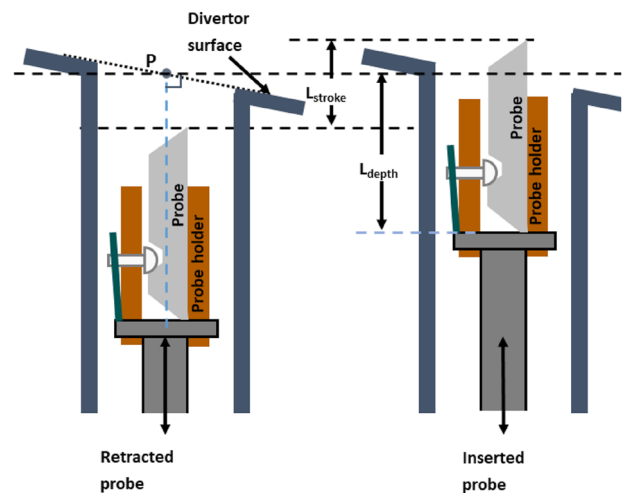$$L_{Probe} = L_{depth} + L_{fin} + l_{optimized}. \quad (4)$$

FIG. 10. Schematic of the retracted and inserted probes in the probe holder.

As shown in Fig. 9, $l_{optimized}$ is the perpendicular distance between the penetration point P and the base of the fin in a situation where the diagonal face of the probe is completely exposed to the SOL magnetic flux tubes and the straight edge of the probe is completely shadowed by the chamfer edge. The value of $l_{optimized}$ can be positive (base of the fin above P) or negative (base of the fin below P) depending upon the angle of magnetic field incidence. A detailed calculation of $l_{optimized}$ for both cases is given in the Appendix.

The final length of the probe was decided based on an optimization, which takes into account all the relevant magnetic field configurations. The actual length ($L_{Probe,act}$) of a probe is the minimum of the probe lengths calculated for all the relevant magnetic field configurations (see Sec. XII). Probes of optimized length are installed in their respective locations in the divertor. The distance between the penetration point and the probe tip in the retracted position of the probes in the divertor was measured. The expected measured distance is ($L_{Probe,act} - L_{depth} - L_{stroke}$). We were able to achieve a remarkable precision in the lengths of the probes with a maximum deviation in the exposed length equal to (0.08 ± 0.01) mm. For most of the probes, the deviation from the desired length was around (0.03 ± 0.01) mm. This deviation in total probe length would translate to a deviation of almost the same value in the projected length, which is well within the desired uncertainty of ± 0.1 mm.

As an outcome of this optimization process, certain magnetic configurations may lead to partial shadowing of a probe's diagonal edge by the chamfered edge of the divertor. This factor needs to be appropriately considered when determining the effective probe area for particle collection, as shown in Sec. XII.

VII. DURABILITY TESTING AND FRICTION TESTS

A W7-X-like magnetic field (~2.5 T) is required to carry out the mechanical testing of the drive coil and electrical contacts (to probes and the coil). The D-MAG experiment device in the University of Greifswald,[35] which has a repurposed gyrotron magnet capable of generating up to 6 T fields, serves as a suitable test-bed for this purpose. A mock-up design of the drive unit and probe assembly was prepared for testing with the original drive coil. The orientation of the coil in the mock-up design was modified to account for the vertical direction of the magnetic field in the D-MAG device. However, the probes and holders were kept vertical (as they are in the original drive unit) to have the same effect of gravity as on the original drive unit. The design of the mock-up drive unit is shown in Fig. 11.

The tests were mainly performed for testing the mechanical strength and durability of the coil assembly, the probe-holders, and the drive unit under the relevant experimental conditions of 2.5 T magnetic field and ultra-high vacuum. Important information about the minimum insertion current and the variation of the speed of the coil with different bias voltage and magnetic field was also obtained through these tests. Scenarios such as deformation of the divertor plates and heating up of the actuator coils were also tested with the mock-up to test the performance of the drive coils in the scenarios with increased friction.

The D-MAG vacuum vessel was heated to 150 °C to simulate the heated environment of the W7-X plasma vessel, and long reciprocation test-runs were carried out with the mock-up. The
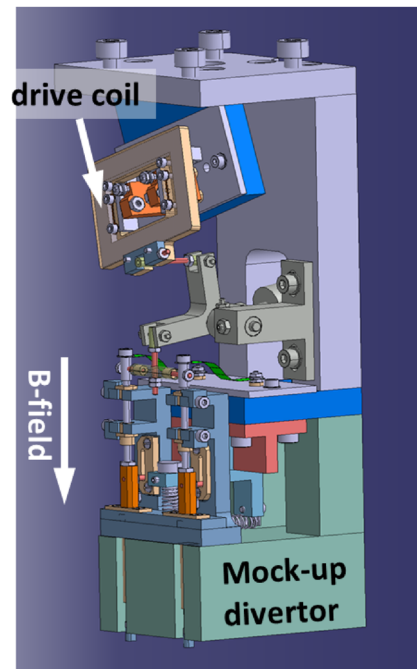

FIG. 11. The mock-up used for the testing of the drive units in the D-MAG laboratory. The coil orientation is made different from Fig. 5 because of the different field direction of the magnet.

temperature of the coil reached 118 °C after four test-runs of 5000 reciprocation cycles each. The increase in temperature was due to the joule heating of the coil and the elevated ambient temperature. The current required for insertion and retraction at higher coil temperatures remained the same as before. However, since the coil resistance had changed, the input voltage was adapted accordingly. The temperature of the coil did not rise significantly even with long test-runs when the D-MAG vessel was not heated. Several waveforms to drive the probes were tested to analyze the motion of the probes through the current and voltage signals. The drive coil was driven for 496 000 reciprocation cycles in total. Due to the difference in coil placement in the mock-up, the friction along the motion of the probes can be different in the mock-up as compared to the original drive units.

The friction tests were conducted individually on the drive units after their installation on the divertors. These tests aimed to determine the friction factors necessary for calculating the insertion current for the drive coils. In these tests, each drive coil was incrementally moved along the insertion path by adding weight to the corresponding arm of the coil. In the lower divertor drives, additional weight is placed on the counter-probe side to facilitate probe movement along the insertion path. Conversely, for the upper divertor drives, extra weight is applied on the probe side for probe movement along the insertion path. The coil was moved along the retraction path by removing the added weight. After every 1 mm vertical displacement of the probe, the total added weight was recorded. The friction and torque on the coil depend on the verti-

03 May 2024 14:53:03

cal displacement s. The torque balance should satisfy the following equation:

$$M_{probe} + M_W(s) = f_i(s)M_c, \qquad (5)$$

where $M_{probe}(s)$ is the moment on the arm of the coil attached to the probe and M_c is the moment on the counter-probe arm. $M_W(s)$ is the moment due to the added weight when the displacement of probe tip from its resting position is s. For upper divertor drive coils, $M_W(s)$ is positive, while for lower divertor drive coils, it is negative. A friction factor $f_i(s)$ (≥ 1) is multiplied with M_c for insertion path.

For retraction direction, the weight applied to the coil was reduced incrementally to bring the coil back to its nominal position,

$$f_r(s)(M_{probe}) + M_W(s) = M_c. \qquad (6)$$

$f_r(s)$ (≥ 1) is the friction factor in the retraction path. The values of f_i and f_s were calculated for each step and averaged to get one average friction factor: f_l and f_u for each lower divertor and upper divertor drive unit, respectively. The range of f_l lies between 1.05 and 1.15, while f_u varies within a range of 1.06 to 1.16.

VIII. COIL CURRENT CALCULATION

The current required for moving the coil and probe system of a drive unit is calculated for a given insertion-time and hold-time. The required current can be calculated by balancing the torque on each side of the coil. The angular acceleration required to move the coil arm such that its linear displacement is s in time t is given by

$$\alpha(t) = \frac{s}{l_p} \frac{2}{t^2}, \qquad (7)$$

and therefore, the torque required is

$$M(t) = I_{coil}\alpha(t) = I_{coil} \frac{s}{l_p} \frac{2}{t^2}, \qquad (8)$$

where s is the vertical displacement of the coil arm or the probe, l_p is the distance from the axis of coil rotation to the location where the probe-holders are attached to the coil, and I_{coil} is the moment of inertia of the coil. In addition to this, a force imbalance on the opposite arms of the coil already exists, which leads to a net torque to keep the probes retracted when no current is applied. This torque is given by

$$M_{rest} = \begin{cases} g[m_c l_c \cos(\gamma + \epsilon) - m_p l_p \cos(\gamma)] & \text{for upper divertor,} \\ g[-m_c l_c + m_p l_p]\cos(\gamma) & \text{for lower divertor,} \end{cases} \qquad (9)$$

where m_p and l_p are the total mass on the probe side and the distance of m_p from the rotation axis and m_c and l_c are the total mass and the distance of the center of mass from the rotation axis on the counter-probe side. For the upper divertor drive units, contrary to the lower divertor drive units, the center of mass location on the counter-probe side is not on the coil. For such a case, the center of mass location on the counter-probe side is shown marked as O in Fig. 12. The point O is inside the counter-weight. Figure 12 shows a simplified 2D geometry for the upper divertor drive unit with the counter-weight. The angle between the line connecting rotational axis of the coil to O and the plane of the coil is ϵ such that
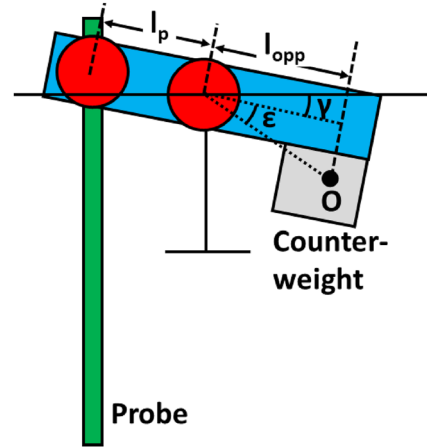

FIG. 12. Simplified schematic of a drive unit as seen from the side (horizontal view in radial direction of the torus). Point O in the counterweight is the center of mass of the counter-probe side.

$l_c = l_{opp}/\cos(\epsilon)$, where l_{opp} is the distance from the rotation axis to the point right above O on the coil.

One can also introduce a friction factor in the expression for M_{rest} as explained in Sec. VII. The friction factor can be estimated from the motional tests done on the drive units after their installation on the divertors. The divertors were not installed inside the W7-X vacuum vessel during the motional tests. These tests were done by adding additional weights on one side of the coil to make the coil move. It was observed that the coil did not start moving even after the theoretical value of the torque balance was achieved. This was because of the static friction opposing the motion. From these tests, an average friction factor (f_l for LD and f_u for UD drive units, its value is typically between 1 and 1.2) is obtained for each drive unit and is included in the expression for M_{rest} before computing the final current values. The friction factor was included in the expression of M_{rest} in a way such that it always increases net torque required to move the coil. The expression of M_{rest} with the friction factor becomes

$$M_{rest} = \begin{cases} g[m_c l_c f_u \cos(\gamma + \epsilon) - m_p l_p \cos(\gamma)] & \text{for UD insertion,} \\ -g[m_c l_c \cos(\gamma + \epsilon) - m_p l_p f_u \cos(\gamma)] & \text{for UD retraction,} \\ g[-m_c l_c + m_p l_p f_l]\cos(\gamma) & \text{for LD insertion,} \\ -g[-m_c l_c f_l + m_p l_p]\cos(\gamma) & \text{for LD retraction.} \end{cases} \qquad (10)$$

The torque produced by a current I through the coil with n turns in a magnetic field B making an angle of $\sim \pm 70^\circ$ (as shown in Fig. 13) with the probe or counter-probe arm and hence with the current direction is given by $\tau_I = nBIA \sin(70^\circ)$.

The final current through the coil for a given insertion time t (or retraction time) is given by solving the following equation:

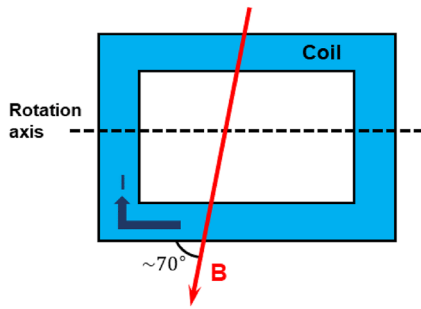$$\tau_I - M_{rest} = M(t). \qquad (11)$$

FIG. 13. Simplified schematic of a drive coil as seen from the top. The magnetic field makes an angle of 70° with the arm of the coil connected to probe or counterweight.

Using Eqs. (8), (10), and (11), we get the following expression for the current required to move the coil:

$$I(t) = \frac{M_{rest} + M(t)}{nBA \sin(70°)}. \tag{12}$$

The appropriate expression for M_{rest} should be chosen according to Eq. (10).

Using the resistance of the circuit, one can calculate the voltage required to move the probes for a given insertion, hold, and retraction time. The resistance of a drive circuit is $R_{circuit}(T) = R_{coil}(T) + R_{contacts} + R_{shunt}$. The resistance of the cable and electrical contacts are included in $R_{contacts}$, and the shunt resistance R_{shunt} is 100 Ω. The coil resistance is sensitive to the temperature (T) of the coil and has a thermal coefficient of resistivity of 0.25 Ω/K. The desired voltage output from the amplifier can be computed by simply multiplying the calculated current from Eq. (12) by the total resistance of the circuit (~264 Ω) at room temperature.

The voltage output from an Analog Output (AO) device is amplified tenfold by an amplifier before going to the drive coil. The temperature of the coil is monitored throughout the operation by calculating the resistance of the coil circuit after each plasma discharge. The current is then adapted to the resistance change of the coil during operation.

IX. CONTROL AND OPERATION OF THE DRIVE UNITS

Each of the drive units is controlled by applying a voltage to the two terminals of its respective coil. Additional connecting cables are available for test use to compare cable resistances with the installed drive units. The voltage to each drive unit is applied by using a power amplifier. The waveforms to each drive unit are calculated based on the desired insertion, hold, and retraction times. For example, a faster insertion would require a greater torque on the coil, and therefore, a larger current and thus a higher input voltage would be needed. The operator of the diagnostic can specify the insertion, hold, and retraction-time for each drive unit separately. The hold time is the duration during which the probe is fully exposed to the plasma. This duration is kept long enough to collect sufficient current–voltage (IV) characteristic curves in one plunge while keeping the temperature of the probe tips under a specified temperature limit. This part of the operation relies on the simulation

of the heating of the probe tips under a given parallel heat flux. The temperature rise of the probe tips in several heat flux scenarios along with the cooling of the tips in parked positions was simulated. Based on these simulations, two quantities critical to operation can be derived. The first is the maximum duration of the probes in the plasma (hold time) for a given heat flux, and the second is the minimum duration between two consecutive plunges (rest time).

A. Drive waveform

Different probes may have different values for hold and rest time depending upon the heat flux received by them. The drive units controlling the probes close to the strike line will have a longer rest time (cooling duration) than the ones further away from the strike line. During operation, the hold time for all the drive units is kept the same at 30 ms. The drive waveforms are supplied by a pre-programmed AO device to the amplifiers, where the signals are amplified ten times. Figure 14 shows a simple waveform, containing the four necessary functional phases. The sequence of events during a plunge is as follows:

a. **Insertion**: Voltage is applied to the coil so that the resulting Lorentz force pushes the probes into the plasma. The probe moves toward the plasma until it hits a mechanical stopper at its fully inserted position, at which point the coil might still be supplying Lorentz force, but the probe does not move.

b. **Hold**: Once the probes are fully inserted in the plasma, they will need to remain in place for a user-specified amount of time to take measurements. If no current is applied to the coil, the probes would fall back to their retracted positions due to the force from a counterweight. Thus, a constant voltage must be applied to the coil during this phase to hold the probes in the plasma against the force of the counterweight. For lower divertor probes, there is no counterweight, but the weight of the probes provides the same effect.

c. **Retraction**: Voltage of the opposite polarity is applied to the coil so that it pulls the probes out of the plasma and holds them there.
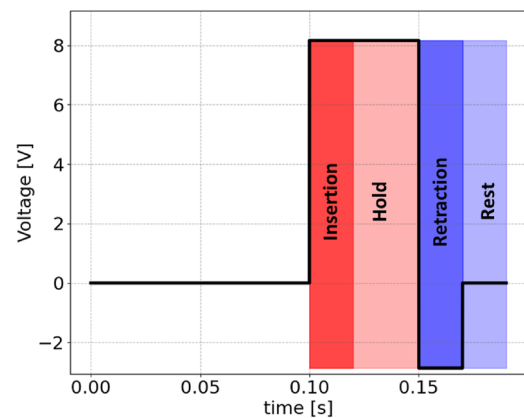

FIG. 14. Waveform for the drive coil showing different phases of drive coil operation.
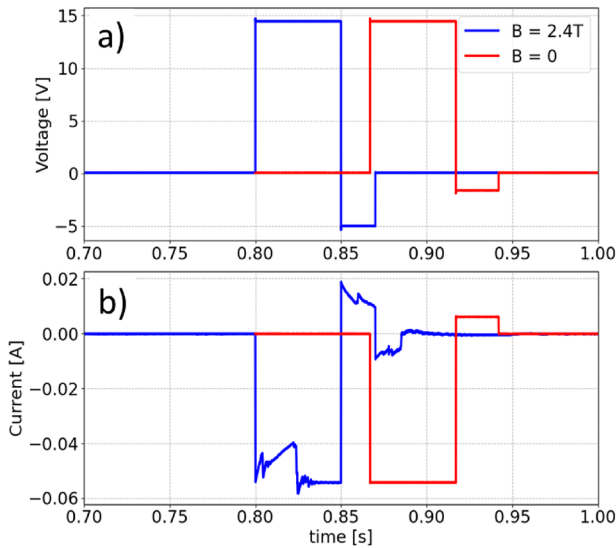
FIG. 15. The input voltage signal to the drive coil circuit (a) and the current in the drive circuit (b) are shown for two cases with and without magnetic fields.

d. **Rest**: No voltage is applied to the coil such that it remains in its retracted position with the help of a co/counterweight.

To determine the coil resistance, a weak voltage can be applied with the retraction polarity. From the voltage and current measurements, the Ohmic resistance of the coil circuit and temperature of the coil can be calculated.

The current flowing through each drive unit yields valuable information about the status of each drive unit and its attached probes. This is because of the induced voltage within the coil as it moves relative to the W7-X field. Figure 15 shows an example of the current flowing through a drive unit [Fig. 15(b)] in response to a voltage signal [Fig. 15(a)] with and without a background magnetic field. The retraction voltages in the two cases are slightly different. In the case without the magnetic field, the coil does not move and the current I is simply proportional to the amplifier output voltage U_{drive} in accordance with Ohm's law: $I = U_{drive}/R_{circuit}$, where $R_{circuit}$ is the total resistance of the drive circuit (coil resistance + cable resistance + shunt resistance ~264 Ω at 20 °C). In the case with the magnetic field, the current signal is lower in magnitude than its no-field level at the beginning of both the insertion and retraction phases. During these times, the coil is moving in response to the Lorentz force, which in turn induces a voltage U_{ind} in the coil against the applied voltage U_{drive} to the circuit. Once the coil hits its stopper and ceases to move, there is no more induced voltage and current signal returns to the same value $I = U_{drive}/R_{circuit}$ (in the hold phase) it reaches in the absence of the magnetic field. With prior knowledge of U_{drive} and $R_{circuit}$, it is simple to calculate the induced voltage: $U_{ind} = U_{drive} - IR_{circuit}$.

To determine the approximate probe displacement over time during its reciprocation, we consider the simple geometry of the upper divertor drive-unit in its fully retracted position, as shown in Figs. 12 and 13. With the coil's movement starting at $t = 0$, there is a consequent change in angle $S(t)$ between the plane of the coil

and the horizontal plane. At a fully retracted position, this angle is shown as $S(t = 0) = \gamma$ in Fig. 12, which reaches zero as the coil aligns with the horizontal plane. Upon complete insertion, the coil experiences an angular displacement of approximately 2γ, which is around 15°. The magnetic field vector is not aligned at right angle to the probe/counter-probe arm of the coil, but at an angle of ~70° (see Fig. 13). The exact value of this angle varies slightly depending on the magnetic configuration and on the location of the probe drive under consideration. The induced voltage in the coil at any time t can be expressed as

$$U_{ind}(t) = -n\frac{d}{dt}[B \sin(70°) \sin(S(t)) \cdot A_{coil}], \quad (13)$$

where n represents the number of turns, B denotes the magnetic field in W7-X, and A_{coil} is the coil's cross-sectional area. Given that $S(t)$ remains within ~−7.5°–7.5°, it is reasonable to approximate $\sin(S(t)) \approx S(t)$. Then, with the knowledge of the magnetic field and the probe geometry, one can calculate the angular displacement $S(t)$ of the coil-arm containing the probe between time $t = 0$ and $t = t_1$ as

$$S(t_1) \approx -\int_0^{t_1} \frac{U_{ind}}{nBA_{coil}} dt. \quad (14)$$

In Eq. (14), we approximate $\sin(70°)$ as roughly equal to 1, making the equation independent of the magnetic configuration used. This approximation is adequate for estimating the displacement of the probe. The result for the lower divertor drive is the same as Eq. (14). This allows the user to monitor the movement of the drive coil and determine at what time instance a probe is fully inserted in the plasma, which is important for the interpretation of the probe current signal. The full linear stroke length of the coil motion is ~5 mm, which is the maximum possible displacement of a probe tip from its resting position. If the distance between the axis of rotation of the coil and the point at which a probe is attached to the coil is l_P, the displacement of the probe tips is ~ $l_P S(t)$. This is also useful for operation and safety, as it indicates whether a drive unit is functioning as desired. Before execution, the programs are checked against a series of compliance parameters to enforce user-defined rules for device safety and data acquisition volume.

B. Control and measurement circuit

The Langmuir probe diagnostic requires 18 control modules to control 18 drive units independent of each other. A simplified control and measurement circuit is shown in Fig. 16.

The waveform specifications are calculated before each plasma discharge depending on the insertion, hold, and retraction times.
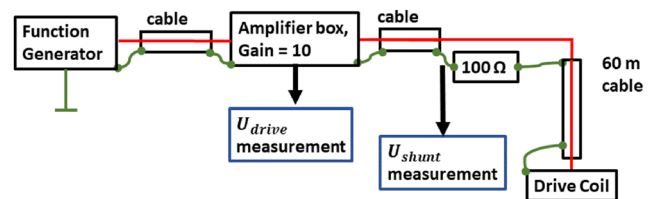

FIG. 16. Simplified circuit for drive unit control and measurement.

The specifications are delivered to an AO device (function generator), which is connected to a power amplifier capable of delivering up to 0.5 A and up to 60 V. The output of the power amplifier is measured and is fed to the drive coils through the drive-cables going to the vacuum vessel. In the return cable path, a 100 Ω resistor is connected in series with the coil and the voltage drop on the resistor is measured. The drive coil has a resistance of ~149 Ω at room temperature. The drive voltage and drive current signals from the measurement card are digitized by using an analog-to-digital converter (ADC) with a sampling rate of 50 kHz and then stored in W7-X Archive. It should be noted that for the operation of the drive coil, the objective is to calculate the drive current rather than the voltage in the drive circuit. The torque on the drive coils is proportional to the current and magnetic field generated by the W7-X field coils. The temperature of the drive coils and hence their Ohmic resistance may vary significantly during plasma operation, and the drive voltage should be adapted to keep the drive current the same in successive plunges.

The basic functional components of the drive unit control as well as the probe biasing and measurement system are shown in Fig. 17. The W7-X timing system (segment control)[36,37] provides a trigger to synchronize the operation of different components of the diagnostic with the W7-X operation. For the pop-up-Langmuir probe diagnostic, this integration of the W7-X segment control and the diagnostic is achieved via a Generic Resource Interface (GeRI).[38] Several diagnostics employed in W7-X make use of GeRI for integration with W7-X segment control. The GeRI software can provide a trigger at a certain desired time interval before the plasma breakdown. At this point, the calculation of the currents required to move each active drive coil is done based on the user specified inputs.

X. CONTROL AND OPERATION OF THE PROBES

As shown in Fig. 17, the probe biasing and measurement are also integrated with W7-X segment control. A biasing AC signal (usually a sine wave with amplitude ±10 V) is created by a function generator and fed to a power amplifier. The power amplifier amplifies the AC signal by ten times. A DC offset of ~ −80 V, generated by a programmable DC power supply, is added to this AC signal to create the biasing signal, which is a sine wave with amplitude ranging from −180 to +20 V. The same analog output card, which is used for controlling drive coils, also provides the input to the programmable DC power supply to generate −80 V. The power amplifier biases probes to the desired amplitude and supplies current (up to 1 A DC with possible 10 μs bursts of 5 A) to the load created by the plasma. The biasing signal is fed to a bridge box. A bridge box contains a reference line and four probe lines. Each of the 36 probes is biased via co-axial probe cables, consisting of one biasing line connected directly to the probe and one return line connected to the vessel. Additional connecting cables are available for test use in comparison with the installed probe circuits.

A. Bridge circuit

A bridge circuit is used for biasing the probes and measurement of the probe signals. The circuit suppresses the effects arising due to the long cable lengths (~60 m) as follows:

(1) The relationship between the measured probe voltage and signal transit time in the cable (τ_R) differs from that of the current and the signal transit time [as shown in Eqs. (15) and (16)], with longer cables exacerbating the time delay between the current and the measured voltage.
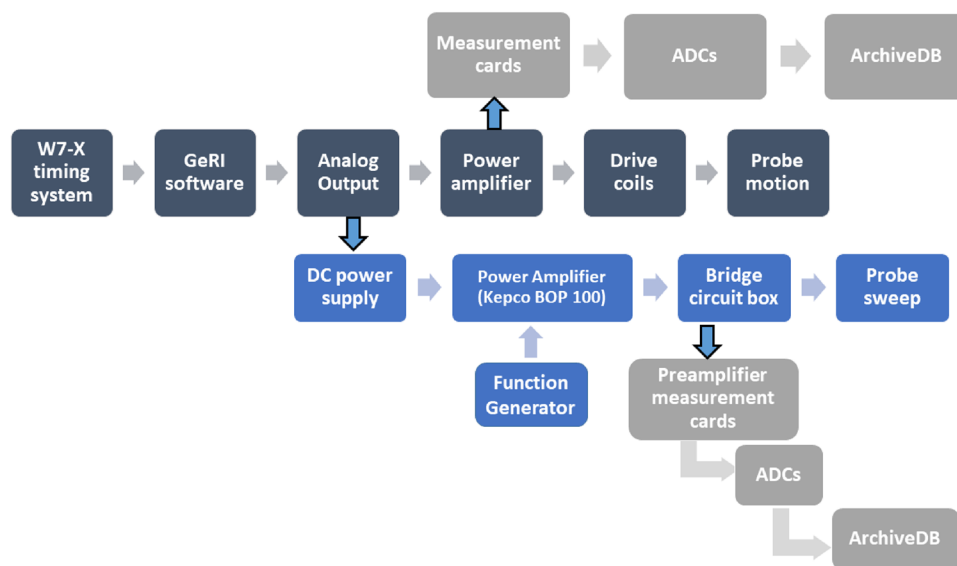
FIG. 17. Complete scheme for the control and data acquisition for the drive coils and the Langmuir probes.
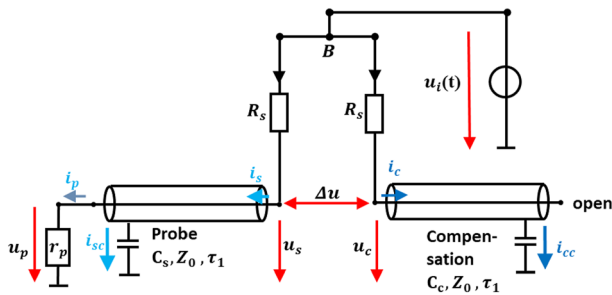
Bridge circuit

FIG. 18. Circuit diagram consisting of a simple bridge circuit with one load (probe) arm.

FIG. 19. Schematic showing all the components in a probe arm of the bridge circuit.

(2) The overall capacitance of the cable, which increases with its length, leads to capacitive influences on the measurements.

The simplest bridge circuit essentially includes two arms in parallel connected to the same input source at the bridge B point, as shown in Fig. 18. The two arms are a load arm and a reference or compensation arm. The compensation arm is of the same length as the load arm. The capacitors shown in Fig. 18 represent the capacitance of the coaxial cables. The other end of the load arm is connected to a load and eventually to ground, whereas the reference arm is kept open so that only a displacement current flows in the compensation arm. The running waves on the long cabling influence the voltage at the bridge point. The voltage at the load differs from the voltage at the bridge. Collecting the bridge input voltage as well as the voltages in both bridge arms makes an excellent correction possible. The effect of load can be obtained by taking the difference of the potential at the input of the probe branch u_s and the potential in the compensation branch u_c. Then, the current in the load arm due to the load can be calculated by using the following simple relation:

$$I_{load} = \Delta u / R_s = (u_s - u_c)/R_s. \quad (15)$$

The expression for calculating the current uses u_s, which is the voltage measured at the input to the probe line. The probe voltage is calculated by using the following expression:[39]

$$u_p(t) = \frac{Z_0 u_i(t - \tau_R)}{Z_0 + R_s}\left(1 + \frac{u_s(t)\frac{Z_0+R_s}{Z_0} - u_i(t)}{u_i(t - 2\tau_R)}\right), \quad (16)$$

where Z_0 is the impedance of the coaxial probe cable or compensation cable, $u_i(t)$ is the input to the bridge circuit at time t, and $\tau_R \sim 0.3 \mu s$ is the signal run-time on the long coaxial cable. The probe voltage obtained using Eq. (16) is used for the LP analysis. For the case without any load in the load arm, this current becomes zero.

Depending on the frequency of operation and current driving limit of the amplifiers, one compensation arm can be used with multiple load arms. For the pop-up probes, each compensation arm was used with a maximum of four probes (the probe–plasma system is the load). In total, ten bridge circuits were used for operating 36 probes. Two bridge circuits were operated with two probes each
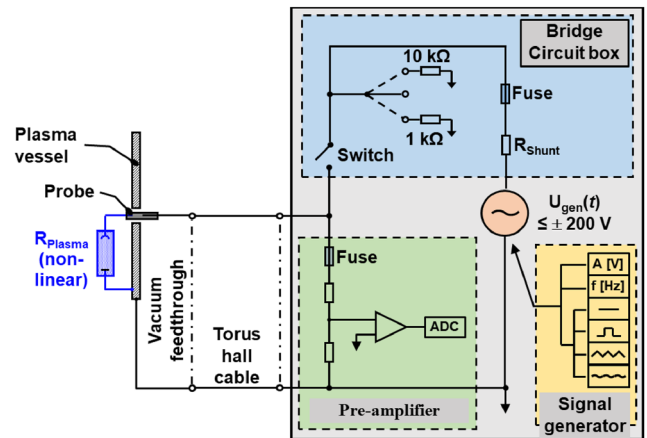
and eight circuits with four probes each. In addition to the components shown in Fig. 18 for a simple bridge, some other components were used in each arm (both compensation and probe arms) for introducing additional features to the circuit. Figure 19 shows a probe arm of the bridge circuit used for pop-up probes. The compensation arm is identical to the probe arm shown in Fig. 19 except that in place of the probe at the end of the arm nothing is connected in the compensation arm. The arm shown in Fig. 19 has a switch to disconnect the bridge circuit from the probe. This allows for the measurement of floating potential when the bridge is disconnected. In addition to this, there is an option to connect the arm to ground via a 1 or 10 kΩ resistor in parallel to the main line. The main line is the cable going to the probe or open end from the power supply. These 1 and 10 kΩ resistors serve two purposes, namely, (a) during a glow discharge, the switch to the resistor is closed and 1 kΩ is connected to the circuit so that a high potential does not develop on the probe; (b) the resistors can be used for troubleshooting without plasma in the case of a problem in the circuit.

The probe signal passes through a preamplifier connected to the measurement card (shown as the OP-amp connected to the ADC in Fig. 19), which measures the bias voltage and floating voltage. The voltage signals from the measurement card go to a digitizer. The digitized signals are sent to the W7-X data archive—ArchiveDB (Fig. 17). The attenuation in the long cables between the bridge circuit and the probes limits the sweeping frequency (f_c) using this approach. Shortening the length between bridge and probe, the cable attenuation can be reduced drastically and the frequency can be increased further. The bridge circuit was already tested during OP 1.2b for two Langmuir probes. Several qualifying tests with long cables of different lengths at frequencies ranging from 500 Hz to 10 kHz had shown the usability of the concept for OP2.1. For OP2.1, the frequency of sweeping was limited to 1 kHz. The cable lengths of the load arm and the compensation arm have to be almost the same for efficiently using the bridge circuit. The effect of cable lengths becomes more crucial for higher sweeping frequencies (>5 kHz). For 1 kHz, the maximum difference in the cable lengths of probe arm and reference arm in one bridge circuit should not exceed 20 cm. Almost equal cable lengths for relevant cables were ensured

03 May 2024 14:53:03

by matching the total capacitance of the cables. The speed of the signal in the cable is $\sim 2 \times 10^8$ m/s, which results in a wavelength of ~200 km for a 1 kHz signal. The cable length is very small as compared to the wavelength, and that is why the compensation works very effectively with 60 m cables. For future campaigns, the bridge circuit could be moved closer to the Langmuir-probe (plasma vessel). This would decrease the attenuation in both bridge arms and allow the increase of the sweeping frequency f_c beyond 50 kHz. In case the wiring becomes longer at higher sweeping frequency, the probe voltage is influenced by the cable run-time.

XI. OPERATION DURING EXPERIMENT PROGRAM

Before operating the diagnostic, a polarity check of the signal generated by the analog output device is done for all the drives without magnetic field. The required insertion/retraction polarity of the input signal for each coil is known beforehand.

A. Operation with magnetic field

With the magnetic field, the drive coils receiving the signals with correct polarity and right amplitude will move. This is checked when the magnetic field of W7-X is on but without the plasma. An illustration depicting the coil signals for one of the drive units during a plasma discharge is presented as an example in Fig. 20. Figure 20 shows the input voltage [Fig. 20(a)] and coil current [Fig. 20(b)] signals for a plunge event along with calculated displacement of the probe from the resting position [Fig. 20(b)]. The input voltage shown in gray in Fig. 20(a) for the drive unit was calculated for an insertion duration of 20 ms. The voltage drop on the drive coil is
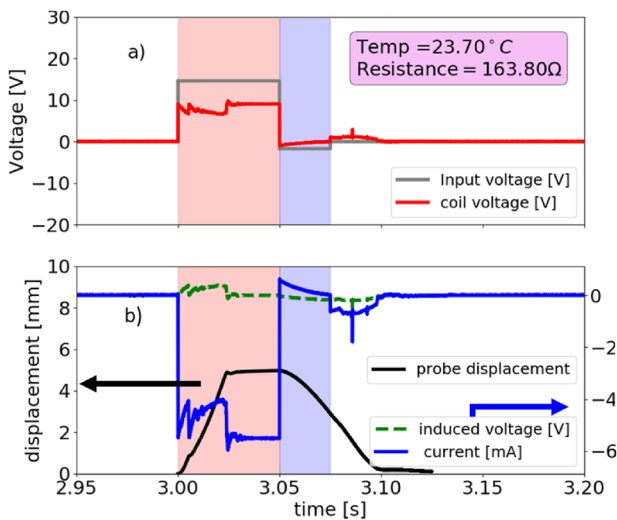

FIG. 20. Summary of a plunge-in of drive 218 in the lower divertor. (a) The input voltage from the amplifier to the drive coil circuit in gray and the voltage drop across the drive coil in red. (b) The linear displacement of the probe tip in black, the current through the circuit in blue, and the induced voltage in the coil in the green dashed line. The current through the coil makes the coil move in the magnetic field of W7-X. This movement is captured in the drive current. The probe displacement remains approximately at 5 mm after the complete insertion and starts decreasing in the retraction phase showing a successful plunge-in.

shown in red. One can see a small change in the drive coil voltage during the insertion phase. At this time, the current signal shows large fluctuations. The deviation in current from $I = U_{coil}/(R_{circuit})$ is because of the induced voltage in the circuit due to the motion of the coil in the magnetic field. The induced voltage U_{ind} is an indication of the motion of the coil and can be used to calculate the displacement of the probes,

$$U_{ind} = U_{drive} - IR_{circuit}. \qquad (17)$$

The calculated temperature of the coil and the value of the resistance $R_{coil} + R_{contacts}$ is also shown in Fig. 20(a).

B. Bridge circuit output calibration with data acquisition software and control

The circuit calibration is done by biasing the probes and acquiring the voltage signals without plasma and without the magnetic field with the probes in parked position. The current calculated from the bridge circuit should be zero in this case. However, the ADCs record a small value, which increases in magnitude linearly with the applied voltage. The slope in the recorded data, as a function of applied voltage from a calibrated source, is a result of finite resistance of the long cables and electrical contacts, which are slightly different in each bridge arm, whereas the intercept is the background noise recorded in the ADC. The calibration parameters can be easily obtained by setting the output current to zero.

The operation of the diagnostic is linked with the segment control of W7-X via an interfacing software GeRI (Generic Resource Interface). The operation program is divided into three main phases: a preparation phase, a run phase, and a post phase. The signals required for the operation of the diagnostic are calculated in the preparation phase and stored in a temporary memory buffer. The plasma heating is on during the run phase, and the coils move the probes into the plasma at desired time instances to acquire the current–voltage characteristic. In the post phase, the heating is switched off and the diagnostic goes into idle mode as the data are being written to the W7-X data archive. The drive waveform parameters pop-up time, insertion time, hold time, and retraction time are set by the operator before the start of the preparation phase. The biasing voltage and data recording are on throughout the discharge.

XII. EFFECTIVE SHEATH AREA

A time trace of the voltage and calibrated current signals recorded by one of the pop-up probes is shown in Fig. 21. The applied voltage signal is from −180 to +20 V at 1 kHz. Typically, the probe insertion time is programmed as 20 ms, followed by a programmed 30 ms duration of probe exposure in the plasma. Observations have shown that the real insertion time often is ~25 ms or less. As a result, the analysis methodology involves evaluating data starting from 25 ms after the onset of insertion and up to 25 ms after the probe has been fully inserted. The current–voltage (I–V) characteristics are obtained as explained in Sec. X.

The I–V curves for the pop-probes near the strike line from one of the standard configuration discharges are shown in Fig. 26. Since the incidence angle on the pop-up probe tips is roughly around 24°, the IV characteristics show the non-saturation of the ion currents,[15,16,40] but the increase in ion current with bias voltage
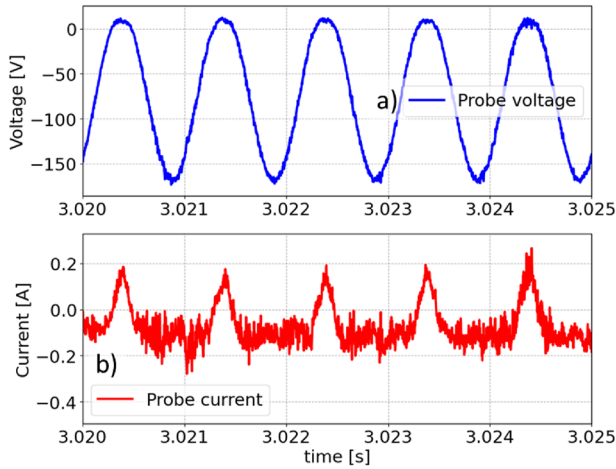
FIG. 21. (a) Voltage and (b) current signals recorded by the pop-up probe on the upper divertor at the strike line location.

FIG. 22. Pop-up probe tip and divertor geometry showing the part of the probe shadowed by the sheath on the divertor and the part, which is exposed to the long flux tubes.

is small and visible clearly only when the current is low. Although the effect of non-saturation of ion current is small, nevertheless, an appropriate sheath expansion model must be applied to obtain meaningful values of the plasma parameters. Since the probes have proud tips and are not flush mounted, the models such as given by Weinlich and Carlson[15] cannot be directly applied to the pop-up probes. The sheath expansion model by Tsui et $al.$[16] does not include the effect of the different extent of magnetic pre-sheaths[41] of the probe and the surrounding wall. To appropriately address the sheath expansion for the pop-up probes, we must subtract the area of the probe sheath, which is shadowed by the sheath on the divertor. The geometry of the probe partially shadowed by the divertor sheath during plasma operation is shown in Fig. 22. Here, the sheath on the probe is not shown for simplifying the geometry, but a sheath is present above the probe as well. First, we want to calculate the part of the probe, which is shadowed by the divertor. In Sec. VI, we had described the calculation of $l_{optimized}$, which is the perpendicular distance between penetration point and the base of the inserted probe fin for a given magnetic configuration, such that the probe of length $L_{Probe} = L_{depth} + L_{fin} + l_{optimized}$ will have its full oblique face presented to the plasma but not the straight edge. This is shown in Fig. 22 as the optimum probe position in the dashed line. The final length of the probe was decided based on an optimization, which takes into account all the relevant magnetic field configurations. As stated in Sec. VI, the actual length of a probe is the minimum of the probe lengths calculated for all the relevant magnetic field configurations. Therefore, the actual probe length might deviate from L_{Probe}. The actual probe position will be a distance δ below the optimum position. We define a length $l_{act} = L_{Probe,act} - L_{depth} - L_{fin}$, where $L_{Probe,act}$ is the actual length of the probe; then,

$$\delta = l_{optimized} - l_{act}. \qquad (18)$$

In Fig. 22, the shadowed part of the probe face is $l_{cut} + l_{sh}$. The thickness of the sheath above the grounded divertor ζ_W is calculated by Weinlich's sheath expansion model for a grounded surface. The projection of ζ_W to the magnetic field is $D_W = \zeta_W \cos(\beta)$, where β is

the angle of incidence of the magnetic field on the divertor surface. The angle of incidence of the magnetic field on the oblique probe face is i. A length $l_{cut} = \delta \sin(\omega)/\sin(i)$ of the probe face is shadowed by the chamfer edge, as shown in Fig. 22. The sheath on the divertor will cast its shadow over a length $l_{Sh} = D_W/\sin(i)$ on the oblique face of the probe. We can now add the next layer of complexity to the problem, which is the sheath on the probe face. The geometry of the probe–divertor sheath is shown in Fig. 23. We have already calculated the shadowed length of the probe face, $l_{shadowed} = l_{cut} + l_{Sh}$. The effective length of the probe becomes $l_{eff} = 2R_P/\cos(\psi) - l_{shadowed}$. The effective length of the sheath exposed to the plasma is given by

$$l_{eff-sheath} = l_{eff} + l_{add}(V_{bias}). \qquad (19)$$

$l_{add}(V_{bias})$ is the length of the probe sheath that should be added to the effective length of the probe to obtain the effective length of the sheath on the diagonal face of the probe. $l_{add}(V_{bias})$ is a function of the bias voltage V_{bias} and is equal to $\zeta_P(V_{bias})\tan(i)$. ζ_P is the sheath thickness on the probe and is calculated from Weinlich's sheath expansion model.[15] The effective area of collection A_{coll} can be easily calculated from the quantities derived thus far,

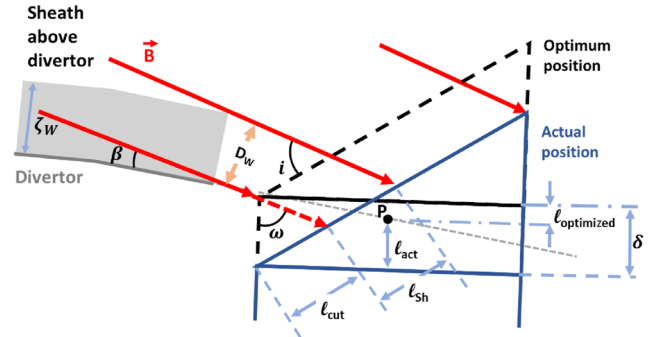$$A_{coll} = (t_{total}l_{eff-sheath} - A_{curv}(1 + f_H)) \sin(i), \qquad (20)$$
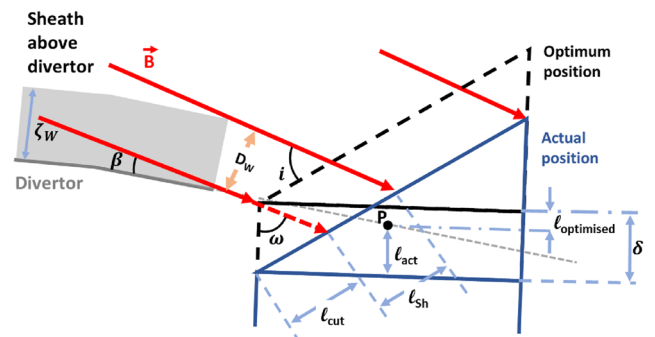

FIG. 23. Pop-up probe tip and divertor geometry showing the part of the probe shadowed by the sheath on the divertor and the part, which is exposed to the long flux tubes along with sheath formed above the probe tip.
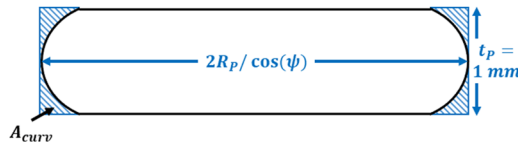
03 May 2024 14:53:03

FIG. 24. A sketch showing the top view of the diagonal face of the probe tip, outlined in black. The shaded areas on each side of the probe face is denoted by A_{curv}. The total area of the probe face is calculated as the area remaining when $A_{curv}(1 + f_H)$ is subtracted from the rectangular area $t_{total}\, l_{eff-sheath}$.

where t_{total} is the total thickness of the probe + sheath geometry = (1 mm + $2\zeta_P$). The Heaviside function f_H is given by $f_H = H(\zeta_P/\tan(i) - l_{shadowed})$. This formulation ensures that the curved area, A_{curv}, from the probe's lower face is subtracted only if the probe sheath from that region is shadowed by the sheath of the divertor. To account for the sheath formation on the lateral sides of the probe face shown in Fig. 24, an additional thickness of $2\zeta_P$ is added to the probe thickness based on the perimeter sheath expansion model described in Ref. 16. The sheath formation on the curved sides of the probe face is not taken into the area calculation. In Fig. 24, the right curved side of the probe face is largely shadowed by the probe tip, while the left curved side is either fully or partially concealed by the sheath over the divertor. The area of the curved part is calculated by the following formula derived from the geometry of the probe face as shown in Fig. 24:

$$A_{curv} = \frac{1}{\cos(\psi)}\left(R_P t_P\left(1 - \frac{1}{2}\cos\Theta\right) - \Theta R_P^2\right) \qquad (21)$$

where $\Theta = \sin^{-1}(0.5 t_P/R_P)$. The calculated area from Eq. (20) is a function of plasma parameters (electron temperature T_e and plasma density n_e) and the bias voltage V_{bias}. Demonstrating the outcome of sheath expansion calculations, Figs. 25(a) and 25(b) illustrate how sheath thickness and sheath area change with the bias voltage applied to probe 1. As depicted in Fig. 25, both sheath thickness and area expand with increasingly negative bias voltage. For comparison, Fig. 25(a) also includes the sheath thickness over the grounded divertor surface, and Fig. 25(b) includes the probe's projected area in the absence of plasma. The sheath expansion with plasma includes the expansion of the sheath on the sides of the probe tip as described above, hence exceeding the probe's projected area with a zero bias voltage.

The expression for the current collected by the LP is given by[16]

$$I_{Probe} = J_{Sat} A_{coll}\left[1 - \exp\left(\frac{e(V_{bias} - V_f)}{T_e}\right)\right]; V < V_{plasma}, \qquad (22)$$

where $V_{plasma} \approx V_f + 3T_e$[40] is the plasma potential. The relationship between current and voltage for Langmuir probe data, as outlined in Eq. (22), is based on the assumption of a Maxwellian electron energy distribution. This assumption is commonly made for the SOL plasma.[15,16,41,42] However, it is not always accurate. In the scrape-off layer of tokamaks and stellarators, a bi-Maxwellian electron distribution is often observed.[5,43–46] In this paper, we maintain the premise of Maxwellian electron behavior. Addressing deviations from the Maxwellian electron energy distribution in the W7-X divertor plasma would require a comprehensive analysis of different
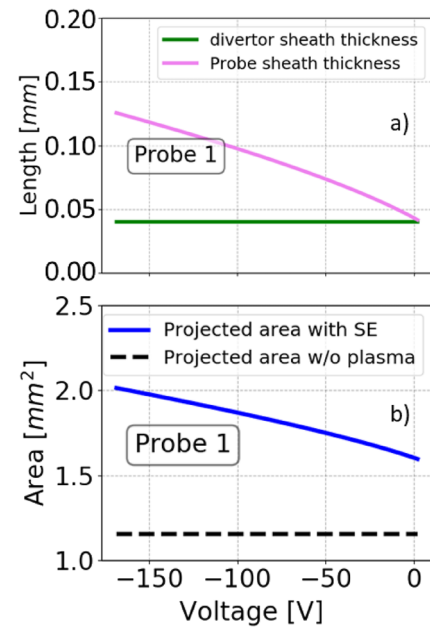

FIG. 25. The variation of sheath thickness above probe 1 as a function of applied voltage and sheath thickness on the grounded divertor is shown in (a). The projected areas of the probe after sheath expansion in plasma and without plasma are shown in (b).

W7-X plasma operation scenarios, a topic that exceeds the scope of this paper and is intended for future research. In high magnetic field environment of fusion devices, applicability of Eq. (22) is reduced where smaller than expected electron currents are observed.[16,47] Moreover, the value of V_{plasma} is not known beforehand. Here, we follow the usual practice for analyzing Langmuir probe characteristic, which is to only use the part of the IV characteristic where the bias voltage is more negative than the floating potential and ignore the net electron collection part.[14,16,42] A value of the floating potential is first obtained from the IV characteristic, and this initial estimate is used to exclude the net electron current part of the IV characteristic. The estimated floating potential value also serves as an initial value of V_f in the iterative fitting of the IV characteristic.

The sheath expansion (SE) model adapted for the pop-up probes is used to generate the curves marked as SE *Fit* in Fig. 26. Figure 26 shows six IV curves for six TM2h probes, which are closer to the strike line than other probes at the same toroidal angle for the "standard" magnetic field configuration of W7-X. Probes 2, 3, and 4 are directly under the strike line. Plasma parameters, namely, electron temperature T_e, plasma density n_e, and floating potential on the probe V_f, are obtained by fitting a sheath expansion model on the experimental IV curves. The density and temperature profiles obtained from the lower divertor probes for an experiment program 20 230 323.030 are shown in Fig. 27 at two time instances $t = 1.8$ s and $t = 6.2$ s. The radiation fraction at these time instances were ~28% and 90%, respectively. One can see the effect of higher radiated power at $t = 6.2$ s on the density and temperature for the probes close to the strike-line-peak, which is at ~5.2 m. For the detached

03 May 2024 14:53:03

plasma case (radiation fraction ~90%), the temperature is reduced below 10 eV near the strike-line as expected.[3,26,48] The probes positioned furthest away from the strike line measure very low densities in the attached as well as detached cases.[49–51]

In the profiles shown in Fig. 27, the data from probe at R = 5.42 m are not shown. During this discharge, the probe at R = 5.42 m deviated from its intended position inside the probe holder, posing challenges in accurately determining its exposed area. While a rough estimate of the probe area can be derived from the current signals, this introduces substantial uncertainties in the ultimate values of density and electron temperatures. There are two more probes at R = 5.52 and 5.55 m on the outboard side at the same ϕ value, which are not included in Fig. 27. Due to the small plasma density on the outboard side, the current signals from these probes were on par with the background noise of the ADCs, rendering a reliable determination of plasma parameters unfeasible.

XIII. SUMMARY

The development, implementation, and successful operation of pop-up Langmuir probes in the W7-X HHF water cooled divertor are described. Fast reciprocation of the divertor Langmuir probes is required in W7-X to avoid heating of the probe tips to unacceptable temperatures. Assiduous engineering design and rigorous testing of the reciprocating system have resulted in a robust probe-driving assembly (drive unit) capable of fast reciprocation for over 400 thousand reciprocation cycles. Nine such drive units are installed each in the upper and lower divertor of module 5 of W7-X. In total, 18 drive units are installed. Two probes are attached to each drive unit. The control of the drive unit is through a voltage signal waveform from an AO device. The operation of the drive units and probes is automated, and the operator has to provide the (1) pop-up time: for when during a plasma discharge the probes should be plunged-in; (2) insertion time: to calculate the speed of insertion and hence the voltage output required from the analog output generator; (3) hold time: to calculate the amplitude of the voltage signal and duration of the signal for which the probes should be exposed to the plasma; and (4) retraction time: to calculate the speed of retraction and hence the voltage output required from the analog output generator. The motion, temperature, and resistance of the moving drive coil can be monitored using the drive voltage and current signals. An important feature of the diagnostic is that the tungsten probes can be replaced if required. The drive units are installed behind the divertor and therefore become inaccessible; therefore, the access to the probes and their replaceability is ensured by the design of the probe holders. The probes have been designed after calculating the length of each probe such that the probes would not present a leading edge in any magnetic configuration where moderate to high heat fluxes are expected on the probe. The maximum projected length of the probe is designed to be (1 ± 0.1) mm for any magnetic field configuration. For the data analysis, a sheath expansion model based on the geometry of the proud Langmuir probe tips and oblique angle of magnetic field incidence on the divertor surface and probes is used. The results obtained from the model fit with experimental observations, indicating that the increase in the collection area is reproduced in the model.

AUTHOR DECLARATIONS

Conflict of Interest

The authors have no conflicts to disclose.

Author Contributions

A. Pandey: Conceptualization (equal); Formal analysis (equal); Investigation (equal); Methodology (equal); Software (equal); Visualization (equal); Writing – original draft (equal). **S. Bohm**: Resources (supporting). **A. Carls**: Investigation (supporting); Resources (supporting). **C. Cordes**: Resources (supporting). **M. Endler**: Conceptualization (equal); Investigation (equal); Methodology (equal); Supervision (equal); Writing – review & editing (equal). **J. Fellinger**: Resources (supporting). **S. Freundt**: Conceptualization (lead); Methodology (equal); Project administration (equal); Resources (equal). **K. Gallowski**: Resources (equal). **K. Hammond**: Conceptualization (equal); Investigation (equal); Resources (equal). **D. Hathiramani**: Conceptualization (equal); Methodology (equal); Project administration (equal); Writing – review & editing (equal). **G. Isberner**: Resources (supporting). **J. P. Kallmeyer**: Conceptualization (equal); Methodology (supporting); Resources (equal). **M. Krause**: Conceptualization (supporting); Resources (supporting). **J. Kügler**: Conceptualization (equal); Methodology (equal); Resources (equal). **M. Otte**: Conceptualization (equal); Project administration (equal); Resources (equal); Software (supporting); Supervision (equal); Writing – review & editing (equal). **T. S. Pedersen**: Project administration (equal); Resources (equal); Supervision (equal). **D. Rondeshagen**: Conceptualization (equal); Methodology (equal); Resources (equal). **J. Ruhnau**: Resources (supporting). **T. Schröder**: Data curation (equal); Software (equal). **T. Sieber**: Conceptualization (supporting); Resources (equal). **J. Wendorf**: Conceptualization (supporting); Resources (supporting).

DATA AVAILABILITY

The data that support the findings of this study are available from the corresponding author upon reasonable request.
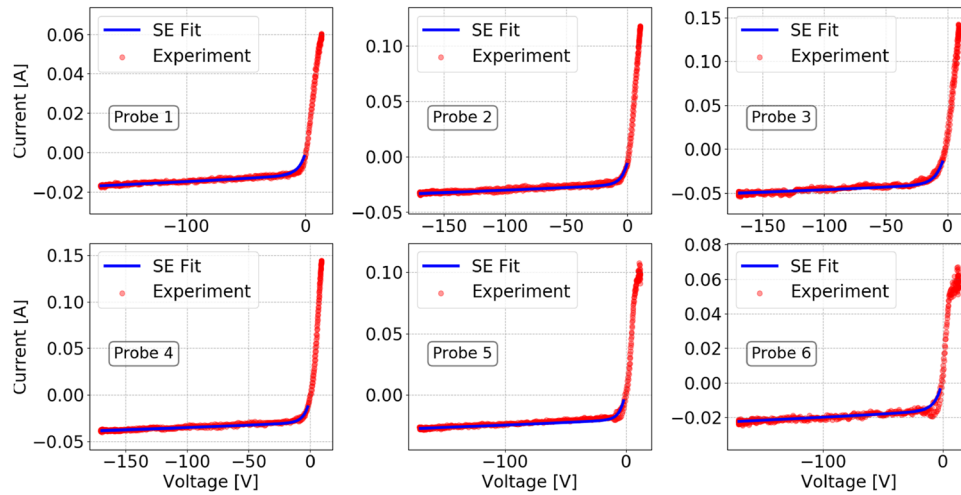
03 May 2024 14:53:03

FIG. 26. IV characteristics for the six pop-up probes in target module 2h of the lower divertor from a "standard configuration" discharge. Every IV curve shown is an average of 25 individual IV curves, collected over a period of 25 ms.
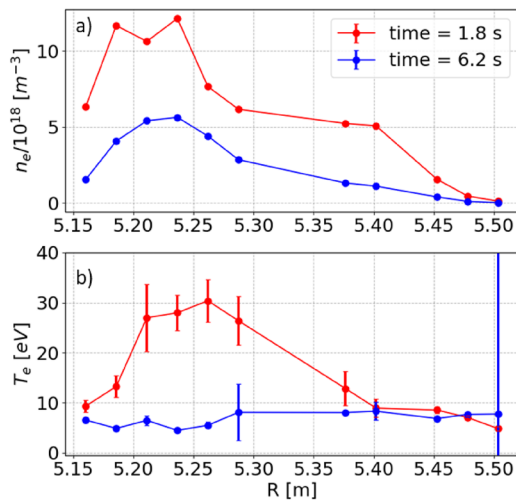

FIG. 27. Profiles of plasma parameters measured by the upper divertor probes in the discharge 20 230 323.030. (a) and (b) The n_e and T_e profiles, respectively, at two time instances. Each measurement point is an average value over 25 ms.

APPENDIX: CALCULATION OF $l_{optimized}$

We consider two situations for magnetic field incidence on the pop-up probes, which are possible in W7-X. First, where the magnetic field is diverging away from the penetration point P as shown in Fig. 28. Figure 28 shows a probe in the initial probe position or *unoptimized* probe position, with the probe length equal to $L_{depth} + L_{fin}$, where $L_{fin} = 2R_p \tan(\psi)$ is the length of the fin, as shown in Fig. 28. In this configuration, a part of the probe is shadowed by the chamfered edge. If a length equal to $l_{optimized}$ is added to the probe length, the fin would be shifted upward and the magnetic field would make contact with the probe at the base of the fin

such that no part of the fin is shadowed. The value of $l_{optimized}$ can be calculated by using the following relation:

$$l_{optimized} = L_{chamfer}\left[\tan(\beta)\cos(\alpha) + \tan(\beta)\sin(\alpha)\tan(\alpha - \beta)\right] - R_p\tan(\beta). \tag{A1}$$

Next, we consider the situation where the magnetic field is converging onto the penetration point as shown in Fig. 29. The unoptimized probe with probe length $L_{depth} + L_{fin}$ is shown in the divertor. This geometry poses a leading edge to the flux tube. In this case, a length should be subtracted from the probe length such that the leading edge is shadowed by the chamfer edge and only the diagonal face of the fin makes contact with the flux tube. As a result of
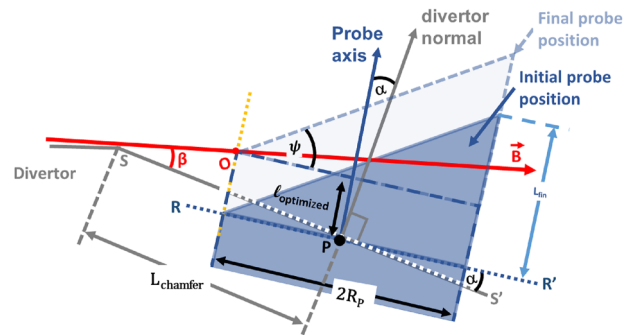

FIG. 28. The case (exaggerated) where the magnetic field is diverging away from the penetration point and an unoptimized probe length is shown installed in the divertor. The inclined edge of the probe face is exposed to the particle and heat flux.
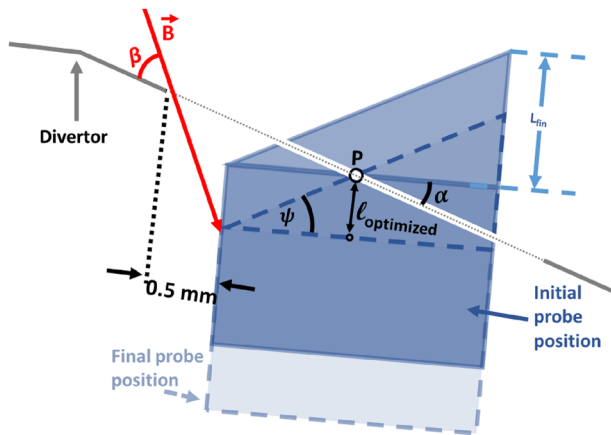
FIG. 29. Exaggerated: The case where the magnetic field is converging onto the penetration point and an "unoptimized" probe is shown installed in the divertor. The straight edge of the probe is exposed to the particle and heat flux. This part of the probe is magnified to show the lengths needed to be calculated to come up with the final length.

this reduction in the length, the value of $l_{optimized}$ is negative, and it is calculated as

$$l_{optimized} = L_{gap}\left[\tan\left(\beta\right)\cos\left(\alpha\right) + \tan\left(\beta\right)\sin\left(\alpha\right)\tan\left(\alpha + \beta\right)\right]$$
$$- R_p \tan\left(\alpha\right). \tag{A2}$$

Given that $l_{optimized}$ may have either a positive or negative value, the overall length of the optimized probe is determined by using the following equation:

$$L_{total} = L_{depth} + L_{fin} + l_{optimized}. \tag{A3}$$

The determination of R_p (= 0.98 mm) was guided by considerations of divertor space and the need to ensure minimal friction during the probe's reciprocating movement. The value of L_{fin} is established using the second optimization criterion, which centers on achieving a projected length of ~1 mm for the probe tip. This projected length, denoted as L_{proj}, is calculated as $L_{proj} = 2R_p \sin\left(\psi + \alpha + \beta\right)/\cos(\psi)$. By setting $L_{proj} = 1$ mm, it becomes feasible to calculate the corresponding ψ values for diverse magnetic configurations (i.e., distinct β values) relevant to a given probe. An average ψ value is derived and standardized for the most frequently employed magnetic configurations specific to that probe. For each individual probe, ψ may vary and falls within the range of $24°$–$33.5°$. The final L_{fin} is $L_{fin} = 2R_p \tan(\psi)$.

The occurrence of either of the aforementioned conditions for a probe depends on the specific magnetic field arrangement. To determine the projected length of the probe, $l_{optimized}$ is computed for each magnetic field setup. From these calculated values, a single $l_{optimized}$ is selected for each probe to establish its individual length. This procedure is carried out independently for each probe. For every probe, a compilation of relevant magnetic configurations is generated. A configuration is considered relevant if the probe experiences substantial heat flux under those magnetic conditions. Among the calculated $l_{optimized}$ values for all pertinent magnetic configurations, the one resulting in the minimum total probe length is chosen for

each specific probe. This process ensures that the probe's length is optimized based on the most crucial magnetic configuration, which corresponds to the scenario where the probe's exposed length was longest in its unoptimized state. This sequence is reiterated for all 36 probes, generating 36 distinct $l_{optimized}$ values. Subsequently, the total probe length is recalculated for each probe using the designated $l_{optimized}$ values, culminating in the final aggregate probe length. Certain probes share identical ψ values, and their total lengths exhibit marginal differences. For these probes, opting for the shortest total length value retains the overall length uncertainty under 0.1 mm. Consequently, the smallest total length value is selected for this group of probes.

REFERENCES

[1] H.-S. Bosch, R. Brakel, T. Braeuer, V. Bykov, P. van Eeten, J.-H. Feist, F. Füllenbach, M. Gasparotto, H. Grote, T. Klinger, H. Laqua, M. Nagel, D. Naujoks, M. Otte, K. Risse, T. Rummel, J. Schacht, A. Spring, T. Sunn Pedersen, R. Vilbrandt, L. Wegener, A. Werner, R. C. Wolf, J. Baldzuhn, C. Biedermann, H. Braune, R. Burhenn, M. Hirsch, U. Höfel, J. Knauer, P. Kornejew, S. Marsen, T. Stange, H. Trimino Mora, and W7-X Team, "Final integration, commissioning and start of the Wendelstein 7-X stellarator operation," Nucl. Fusion **57**, 116015 (2017).

[2] E. Faudot, A. C. Mana, F. Brochard, and S. Heuraux, "Effect of the electrode/wall area ratio on the plasma potential in discharge and tokamak plasmas," IEEE Trans. Plasma Sci. **50**, 799–809 (2022).

[3] P. C. Stangeby, "Basic physical processes and reduced models for plasma detachment," Plasma Phys. Controlled Fusion **60**, 044022 (2018).

[4] R. Dejarnac, D. Sestak, J. P. Gunn, M. Firdaouss, H. Greuner, J.-Y. Pascal, M. Richou, and H. Roche, "Flush-mounted Langmuir probes in the WEST tokamak divertor," Fusion Eng. Des. **163**, 112120 (2021).

[5] T. K. Popov, M. Dimitrova, P. Ivanova, J. Kovačič, T. Gyergyek, R. Dejarnac, J. Stöckel, M. A. Pedrosa, D. López-Bruna, and C. Hidalgo, "Advances in Langmuir probe diagnostics of the plasma potential and electron-energy distribution function in magnetized plasma," Plasma Sources Sci. Technol. **25**, 033001 (2016).

[6] T. S. Pedersen, R. König, M. Krychowiak, M. Jakubowski, J. . Baldzuhn, S. Bozhenkov, G. Fuchert, A. Langenberg, H. Niemann, D. Zhang, K. Rahbarnia, H.-S. Bosch, Y. Kazakov, S. Brezinsek, Y. Gao, and N. Pablant, "First results from divertor operation in Wendelstein 7-X," Plasma Phys. Controlled Fusion **61**, 014035 (2018).

[7] L. Rudischhauser, M. Endler, U. Höfel, K. C. Hammond, J. P. Kallmeyer, and B. D. Blackwell, "The Langmuir probe system in the Wendelstein 7-X test divertor," Rev. Sci. Instrum. **91**, 063505 (2020).

[8] K. C. Hammond, Y. Gao, M. Jakubowski, C. Killer, H. Niemann, L. Rudischhauser, A. Ali, T. Andreeva, B. D. Blackwell, K. J. Brunner, B. Cannas, P. Drewelow, P. Drews, M. Endler, Y. Feng, J. Geiger, O. Grulke, J. Knauer, S. Klose, S. Lazerson, M. Otte, F. Pisano, U. Neuner, A. P. Sitjes, K. Rahbarnia, J. Schilling, H. Thomsen, G. A. Wurden, and W7-X Team, "Drift effects on W7-X divertor heat and particle fluxes," Plasma Phys. Controlled Fusion **61**, 125001 (2019).

[9] M. Endler, J. Baldzuhn, C. D. Beidler, H.-S. Bosch, S. Bozhenkov, B. Buttenschön, A. Dinklage, J. Fellinger, Y. Feng, G. Fuchert, Y. Gao, J. Geiger, O. Grulke, D. Hartmann, M. Jakubowski, R. König, H. P. Laqua, S. Lazerson, P. McNeely, D. Naujoks, U. Neuner, M. Otte, E. Pasch, T. Sunn Pedersen, V. Perseo, A. Puig Sitjes, K. Rahbarnia, N. Rust, O. Schmitz, A. Spring, T. Stange, A. von Stechow, Y. Turkin, E. Wang, and R. C. Wolf, "Wendelstein 7-X on the path to long-pulse high-performance operation," Fusion Eng. Des. **167**, 112381 (2021).

[10] J. Boscary, A. Peacock, R. Stadler, B. Mendelevitch, H. Tittes, J. Tretter, M. Smirnow, and C. Li, "Actively water-cooled plasma facing components of the Wendelstein 7-X stellarator," Fusion Sci. Technol. **64**, 263–268 (2013).

[11] J. G. Watkins, J. Hunter, B. Tafoya, M. Ulrickson, R. D. Watson, R. A. Moyer, J. W. Cuthbertson, G. Gunner, R. Lehmer, P. Luong, D. N. Hill, M. Mascaro, J. I.

Robinson, R. Snider, and R. Stambaugh, "Fast reciprocating Langmuir probe for the DIII-D divertor," Rev. Sci. Instrum. **68**, 373–376 (1997).

[12] J. Boedo, D. Gray, L. Chousal, R. Conn, B. Hiller, and K. H. Finken, "Fast scanning probe for tokamak plasmas," Rev. Sci. Instrum. **69**, 2663–2670 (1998).

[13] M. A. Pedrosa, A. López-Sánchez, C. Hidalgo, A. Montoro, A. Gabriel, J. Encabo, J. de la Gama, L. M. Martinez, E. Sánchez, R. Pérez, and C. Sierra, "Fast movable remotely controlled Langmuir probe system," Rev. Sci. Instrum. **70**, 415–418 (1999).

[14] G. F. Matthews, S. J. Fielding, G. M. McCracken, C. S. Pitcher, P. C. Stangeby, and M. Ulrickson, "Investigation of the fluxes to a surface at grazing angles of incidence in the tokamak boundary," Plasma Phys. Controlled Fusion **32**, 1301 (1990).

[15] M. Weinlich and A. Carlson, "Flush mounted Langmuir probes in an oblique magnetic field," Phys. Plasmas **4**, 2151–2160 (1997).

[16] C. K. Tsui, J. A. Boedo, P. C. Stangeby, and TCV Team, "Accounting for Debye sheath expansion for proud Langmuir probes in magnetic confinement fusion plasmas," Rev. Sci. Instrum. **89**, 013505 (2018).

[17] P. C. Stangeby, "The Chodura sheath for angles of a few degrees between the magnetic field and the surface of divertor targets and limiters," Nucl. Fusion **52**, 083012 (2012).

[18] J. Moritz, M. Lesur, E. Faudot, S. Devaux, S. Heuraux, and J. Ledig, "The plasma-wall transition with collisions and an oblique magnetic field: Reversal of potential drops at grazing incidences," Phys. Plasmas **26**, 013507 (2019).

[19] A. Geraldini, F. I. Parra, and F. Militello, "Gyrokinetic treatment of a grazing angle magnetic presheath," Plasma Phys. Controlled Fusion **59**, 025015 (2017).

[20] P. C. Stangeby, "Large probes in tokamak scrape-off plasmas. Analytic model for the collisionless scrape-off plasma," Phys. Fluids **28**, 644–651 (1985).

[21] S. J. Davies, X. Tellier, G. F. Matthews, and C. H. Wilson, "Development of popup Langmuir probe system for the JET MkIIa divertor," Fusion Eng. Des. **46**, 27–35 (1999).

[22] N. Smick, B. LaBombard, and C. S. Pitcher, "Plasma profiles and flows in the high-field side scrape-off layer in Alcator C-Mod," J. Nucl. Mater. **337–339**, 281–285 (2005).

[23] N. Smick and B. LaBombard, "Wall scanning probe for high-field side plasma measurements on Alcator C-Mod," Rev. Sci. Instrum. **80**, 023502 (2009).

[24] J. Boscary, R. Stadler, A. Peacock, F. Hurd, A. Vorköper, B. Mendelevitch, A. Cardella, H. Pirsch, H. Tittes, J. Tretter, C. Li, H. Greuner, and M. Smirnow, "Design and technological solutions for the plasma facing components of WENDELSTEIN 7-X," Fusion Eng. Des. **86**, 572–575 (2011), part of the Special Issue: Proceedings of the 26th Symposium of Fusion Technology (SOFT-26).

[25] R. Stadler, A. Vorköper, J. Boscary, A. Cardella, F. Hurd, C. Li, B. Mendelevitch, A. Peacock, and H. Pirsch, "The in-vessel components of the experiment WENDELSTEIN 7-X," Fusion Eng. Des. **84**, 305–308 (2009), part of the Special Issue: Proceeding of the 25th Symposium on Fusion Technology.

[26] M. Jakubowski, M. Endler, Y. Feng, Y. Gao, C. Killer, R. König, M. Krychowiak, V. Perseo, F. Reimold, O. Schmitz, T. S. Pedersen, S. Brezinsek, A. Dinklage, P. Drewelow, H. Niemann, M. Otte, M. Gruca, K. Hammond, T. Kremeyer, M. Kubkowska, S. Jabłoński, A. Pandey, G. Wurden, D. Zhang, S. Bozhenkov, D. Böckenhoff, C. P. Dhard, J. Baldzuhn, D. Gradic, F. Effenberg, P. Kornejew, S. Lazerson, J. Lore, D. Naujoks, A. Puig Sitjes, G. Schlisio, M. Śleczka, U. Wenzel, V. Winters, and W7-X Team, "Overview of the results from divertor experiments with attached and detached plasmas at Wendelstein 7-X and their implications for steady-state operation," Nucl. Fusion **61**, 106003 (2021).

[27] Y. Gao, J. Geiger, M. W. Jakubowski, P. Drewelow, M. Endler, K. Rahbarnia, S. Bozhenkov, M. Otte, Y. Suzuki, Y. Feng, H. Niemann, F. Pisano, A. Ali, A. Puig Sitjes, M. Zanini, H. Laqua, T. Stange, S. Marsen, T. Szepesi, D. Zhang, C. Killer, K. Hammond, S. Lazerson, B. Cannas, H. Thomsen, T. Andreeva, U. Neuner, J. Schilling, A. Knieps, M. Rack, Y. Liang, and W7-X Team, "Effects of toroidal plasma current on divertor power depositions on Wendelstein 7-X," Nucl. Fusion **59**, 106015 (2019).

[28] T. Andreeva, J. Geiger, A. Dinklage, G. Wurden, H. Thomsen, K. Rahbarnia, J. C. Schmitt, M. Hirsch, G. Fuchert, C. Nührenberg, A. Alonso, C. D. Beidler,

M. N. A. Beurskens, S. Bozhenkov, R. Brakel, C. Brandt, V. Bykov, M. Grahl, O. Grulke, C. Killer, G. Kocsis, T. Klinger, A. Krämer-Flecken, S. Lazerson, M. Otte, N. Pablant, J. Schilling, T. Windisch, and W7-X Team, "Magnetic configuration scans during divertor operation of Wendelstein 7-X," Nucl. Fusion **62**, 026032 (2022).

[29] K. Krieger, T. Lunt, R. Dux, A. Janzer, A. Kallenbach, H. W. Müller, R. Neu, T. Pütterich, and V. Rohde, "Induced tungsten melting events in the divertor of ASDEX Upgrade and their influence on plasma performance," J. Nucl. Mater. **415**, S297–S300 (2011), part of the Special Issue: Proceedings of the 19th International Conference on Plasma-Surface Interactions in Controlled Fusion.

[30] D. Naujoks, *Plasma-Material Interaction in Controlled Fusion*, *Springer Series on Atomic, Optical, and Plasma Physics* (Springer, Berlin, Heidelberg, 2006).

[31] A. Geier, H. Maier, R. Neu, K. Krieger, and ASDEX Upgrade Team, "Determination of the tungsten divertor retention at ASDEX Upgrade using a sublimation probe," Plasma Phys. Controlled Fusion **44**, 2091 (2002).

[32] D. Naujoks, J. Roth, K. Krieger, G. Lieder, and M. Laux, "Erosion and redeposition in the ASDEX Upgrade divertor," J. Nucl. Mater. **210**, 43–50 (1994).

[33] A. V. Demura, M. B. Kadomtsev, V. S. Lisitsa, and V. A. Shurygin, "Electron impact ionization of tungsten ions in a statistical model," JETP Lett. **101**, 85–88 (2015).

[34] D. E. Post, R. V. Jensen, C. B. Tarter, W. H. Grasberger, and W. A. Lokke, "Steady-state radiative cooling rates for low-density, high-temperature plasmas," At. Data Nucl. Data Tables **20**, 397–439 (1977).

[35] B. Jagielski, U. Wenzel, T. Sunn Pedersen, A. Melzer, A. Pandey, F. Mackel, and W7-X Team, "D-Mag—A laboratory for studying plasma physics and diagnostics in strong magnetic fields," J. Instrum. **18**, P06006 (2023).

[36] H. Laqua, T. Bluhm, M. Grahl, M. Grün, C. Hennig, A. Holtz, J. Krom, G. Kühner, M. Lewerentz, H. Riemann, J. Schacht, A. Spring, and A. Werner, "Experiences with the Segment Control system at Wendelstein 7-X operation," Fusion Eng. Des. **123**, 588–592 (2017).

[37] A. Spring, T. Bluhm, M. Grahl, M. Grün, C. Hennig, A. Holtz, J. Krom, G. Kühner, H. Laqua, M. Lewerentz, H. Riemann, and A. Werner, "Establishing the Wendelstein 7-X steady state plasma control and data acquisition system during the first operation phase," Fusion Eng. Des. **123**, 579–583 (2017).

[38] A. Winter, T. Bluhm, H.-S. Bosch, K. Brandt, S. Dumke, M. Grahl, M. Grün, A. Holtz, H. Laqua, M. Lewerentz, D. Makowski, S. Pingel, H. Riemann, J. Schacht, K. Schaumann, A. Spring, and S. Valet, "Preparation of W7-X CoDaC for OP2," IEEE Trans. Plasma Sci. **48**, 1779–1782 (2020).

[39] J. P. Kallmeyer, "High speed Langmuir data collection with extremely long cabling," Internal Report Nos. IPP-IDM and IPP_28CU7U, 2020.

[40] P. C. Stangeby, *The Plasma Boundary of Magnetic Fusion Devices*, *Series in Plasma Physics and Fluid Dynamics* (Taylor & Francis, 2000).

[41] R. Chodura, "Plasma–wall transition in an oblique magnetic field," Phys. Fluids **25**, 1628–1633 (1982).

[42] P. C. Stangeby, "Effect of bias on trapping probes and bolometers for Tokamak edge diagnosis," J. Phys. D: Appl. Phys. **15**, 1007 (1982).

[43] T. S. V. K. Popov, M. Dimitrova, M. A. Pedrosa, D. López-Bruna, J. Horacek, J. Kovačič, R. Dejarnac, J. Stöckel, M. Aftanas, P. Böhm, P. Bílková, C. Hidalgo, and R. Panek, "Bi-Maxwellian electron energy distribution function in the vicinity of the last closed flux surface in fusion plasma," Plasma Phys. Controlled Fusion **57**, 115011 (2015).

[44] P. C. Stangeby, "A problem in the interpretation of tokamak Langmuir probes when a fast electron component is present," Plasma Phys. Controlled Fusion **37**, 1031 (1995).

[45] C. Killer, P. Aleynikov, C. Biedermann, C. P. Dhard, P. Drews, Y. Gao, O. Grulke, M. Jakubowski, A. Knieps, G. Kocsis, D. Naujoks, A. Puig Sitjes, M. Spolaore, T. Stange, T. Szepesi, A. Tancetti, and H. Thomsen, "Observation of non-thermal electrons outside the SOL in the Wendelstein 7-X stellarator," Nucl. Mater. Energy **33**, 101274 (2022).

[46] D. Tskhakaya, S. Jachmich, T. Eich, and W. Fundamenski, "Interpretation of divertor Langmuir probe measurements during the ELMs at JET," J. Nucl. Mater. **415**, S860–S864 (2011).

[47] J. A. Tagle, P. C. Stangeby, and S. K. Erents, "Errors in measuring electron temperatures using a single Langmuir probe in a magnetic field," Plasma Phys. Controlled Fusion **29**, 297 (1987).

[48] Y. Feng, M. Jakubowski, R. König, M. Krychowiak, M. Otte, F. Reimold, D. Reiter, O. Schmitz, D. Zhang, C. D. Beidler, C. Biedermann, S. Bozhenkov, K. J. Brunner, A. Dinklage, P. Drewelow, F. Effenberg, M. Endler, G. Fuchert, Y. Gao, J. Geiger, K. C. Hammond, P. Helander, C. Killer, J. Knauer, T. Kremeyer, E. Pasch, L. Rudischhauser, G. Schlisio, T. Sunn Pedersen, U. Wenzel, V. Winters, and W7-X Team, "Understanding detachment of the W7-X island divertor," Nucl. Fusion **61**, 086012 (2021).

03 May 2024 14:53:03